

Response of a laminar separation bubble to impulsive forcing

Michelis, T.; Yarusevych, Serhiy; Kotsonis, Marios

DOI 10.1017/jfm.2017.217

Publication date 2017

Document Version
Accepted author manuscript
Published in
Journal of Fluid Mechanics

Citation (APA)

Michelis, T., Yarusevych, S., & Kotsonis, M. (2017). Response of a laminar separation bubble to impulsive forcing. *Journal of Fluid Mechanics*, *820*, 633-666. https://doi.org/10.1017/jfm.2017.217

Important note

To cite this publication, please use the final published version (if applicable). Please check the document version above.

Copyright

Other than for strictly personal use, it is not permitted to download, forward or distribute the text or part of it, without the consent of the author(s) and/or copyright holder(s), unless the work is under an open content license such as Creative Commons.

Takedown policy

Please contact us and provide details if you believe this document breaches copyrights. We will remove access to the work immediately and investigate your claim.

Response of a laminar separation bubble to impulsive forcing

Theodoros Michelis¹†, Serhiy Yarusevych² and Marios Kotsonis¹

¹Department of Aerodynamics, Delft University of Technology, The Netherlands ²Department of Mechanical and Mechatronics Engineering, University of Waterloo, Canada

(Received xx; revised xx; accepted xx)

The spatial and temporal response characteristics of a laminar separation bubble to impulsive forcing are investigated by means of time-resolved particle image velocimetry and linear stability theory. A two-dimensional impulsive disturbance is introduced with an AC dielectric barrier discharge plasma actuator, exciting pertinent instability modes and ensuring flow development under environmental disturbances. Phase-averaged velocity measurements are employed to analyse the effect of imposed disturbances at different amplitudes on the laminar separation bubble. The impulsive disturbance develops into a wave packet that causes rapid shrinkage of the bubble in both upstream and downstream directions. This is followed by bubble bursting, during which the bubble elongates significantly, while vortex shedding in the aft part ceases. Duration of recovery of the bubble to its unforced state is independent of the forcing amplitude. Quasi-steady linear stability analysis is performed at each individual phase, demonstrating reduction of growth rate and frequency of the most unstable modes with increasing forcing amplitude. Throughout the recovery, amplification rates are directly proportional to the shape factor. This indicates that bursting and flapping mechanisms are driven by altered stability characteristics due to variations in incoming disturbances. The emerging wave packet is characterised in terms of frequency, convective speed and growth rate, with remarkable agreement between linear stability theory predictions and measurements. The wave packet assumes a frequency close to the natural shedding frequency, while its convective speed remains invariant for all forcing amplitudes. The stability of the flow changes only when disturbances interact with the shear layer breakdown and reattachment processes, supporting the notion of a closed feedback loop. The results of this study shed light on the response of laminar separation bubbles to impulsive forcing, providing insight into the attendant changes of flow dynamics and the underlying stability mechanisms.

Key words: keywords added during submission

1. Introduction

A laminar boundary layer developing along an aerodynamic surface may separate if exposed to sufficiently strong adverse pressure gradient. Under certain conditions, the increase of momentum exchange due to laminar to turbulent transition in the separated shear layer may lead to reattachment. Therefore, in the time-average sense, a closed recirculation region forms near the surface, namely a laminar separation bubble (LSB, Gaster 1967).

Due to the requirement of a laminar boundary layer state at the separation location, this phenomenon is usually observed at low to moderate Reynolds numbers, typical in applications such as glider or unmanned aerial vehicle wings and turbomachine blades. The transition process associated with LSBs is highly susceptible to environmental disturbances and the resulting separated shear layers are inherently unstable. As a result, changes in background disturbances can lead to unwanted impact on aerodynamic performance such as stalling, loss of lift, increase of drag and noise emission. Due to these implications, numerous studies have been performed to investigate and predict LSB dynamic properties and stability characteristics (e.g. Gaster & Grant 1975; Dovgal et al. 1994; Watmuff 1999). Although applications primarily involve aerofoils, LSBs driven by adverse pressure gradient on semi-infinite flat plates exhibit the relevant fundamental effects and have been used as a suitable experimentation and computation platform (e.g. Gaster 1967; Marxen & Rist 2010).

Whether numerical or experimental, most studies that investigate stability characteristics involve artificial forcing of the boundary layer with known perturbations at a location upstream of the LSB separation point and describe the subsequent flow evolution. The most common type of forcing is sinusoidal and periodic at the most unstable frequency of the separated shear layer, usually identified through linear stability theory (LST) analysis. This type of forcing has been introduced by various means including spanwise uniform wall oscillation (Alam & Sandham 2000; Marxen et al. 2009), externally imposed acoustic excitation (Yarusevych et al. 2007; Jones et al. 2010) as well as DBD plasma actuation (Yarusevych & Kotsonis 2017). However, the majority of the previous studies considered the response of the LSB to continuous forcing. Gaster & Grant (1975) were the first to introduce an impulsive disturbance, exciting the full spectrum of instability modes, thus generating a wave packet through selective amplification. This method was subsequently used by Watmuff (1999) and Diwan & Ramesh (2009). It must be noted that impulsive disturbances have, so far, been locally introduced at a single point, usually a pressure tap. Consequently, the emerging wave packets initially exhibit strong three-dimensional features, which complicates the elucidation of the underlying physical mechanisms and application of LST. The present study, instead, focuses on two-dimensional spanwise-uniform impulsive disturbances.

In the laminar part of the LSB, flow is essentially considered two-dimensional and parallel. If, in addition, small perturbations to the baseline flow are assumed, it is possible to apply linear stability theory for estimating the most amplified unstable mode frequency. Häggmark et al. (2001), Rist & Maucher (2002) and Marxen & Rist (2010) demonstrated that LST applied to the mean baseline flow can successfully reproduce experimental and numerical stability observations. It is generally accepted that disturbances developing in a LSB are initially convectively amplified via a Kelvin-Helmholtz instability mechanism, similar to free shear layers (Ho & Huerre 1984; Watmuff 1999; Marxen et al. 2015). Inviscid inflectional and Göertler type instability mechanisms have been proposed by Diwan & Ramesh (2009) and Marxen et al. (2009) respectively. Furthermore, Theofilis et al. (2000) conjectured a self-exciting, globally unstable process in a disturbancefree numerical environment. In practice, convective amplification of disturbances in the separated shear layer leads to the formation of initially two-dimensional vortical structures which manifest as coherent vortex shedding (Jones et al. 2008; Hain et al. 2009; Serna & Lázaro 2014; Kurelek et al. 2016). Once they reach the aft part of the LSB, these spanwise structures undergo three-dimensional breakdown, the underlying mechanism of which is the subject of active investigations. Marxen et al. (2013) summarise three instability mechanisms that can take place in LSBs: "primary global", "secondary" and "highly localised" instabilities. Primary global instabilities refer to the entire bubble and are typically of low frequency. For a fully global instability to develop, Theofilis (2011) reports a requirement of reverse flow on the order of 10% of the freestream velocity. On the other hand, Alam & Sandham (2000) report that reverse flow between 15% and 20% is required for a local absolute instability. Secondary instabilities are absolute and involve vortex shedding. They are either elliptic, causing three-dimensional deformation of vortex cores, or hyperbolic, affecting the braid region between two consecutive vortices. Finally, highly localised instabilities are of small scale and manifest in high-shear layers. They have been shown to play a role in hairpin vortex formation (Bake et al. 2002).

Rist & Augustin (2006) and Marxen & Rist (2010) documented enhanced flow stabilisation with increasing forcing amplitudes. Additionally, they observed reduction of the LSB size from both upstream and downstream directions. Similarly to Dovgal et al. (1994) and Boiko et al. (2002), they suggested a feedback loop process to explain the bubble size reduction due to controlled disturbances. More specifically, a disturbance input alters the flow in the aft part of the bubble, resulting in a global change of pressure gradient due to viscous-inviscid interactions. This indirectly distorts the mean flow at the upstream part of the bubble towards a more stable state, mitigating subsequent disturbance amplification, effectively leading to stabilisation. Marxen & Henningson (2011) argued that, if irregular disturbances are present in the incoming flow, such as freestream turbulence in free flight or wind-tunnel experiments, the aforementioned feedback loop may explain the occurrence of an intermittent shear layer fluctuation associated with LSBs, often referred to as "flapping" (e.g. Zaman et al. 1989). Adding to this argumentation, significant reduction of the flapping behaviour due to artificial monochromatic forcing has been noted by Dovgal & Boiko (1994) and Sandham (2008), related to the locking of the bubble dynamics to modes of constant amplitude. Moreover, flow stabilisation due to the mean flow deformation under continuous forcing has recently been confirmed experimentally by Yarusevych & Kotsonis (2017).

Laminar separation bubbles are often classified in literature as "short" or "long" based on their length or whether their influence on pressure distribution is global or local (Owen & Klanfer 1955; Tani 1964; Gaster 1967). A detailed overview of the associated bubble characteristics is given by Marxen & Henningson (2011). Pauley et al. (1990) noted that long separation bubbles with laminar reattachment do not exhibit formation of vortex shedding. In contrast, the long separation bubbles of Gaster (1967) and Marxen & Henningson (2011) exhibit laminar to turbulent transition and turbulent reattachment. However, they fail to reattach as early as short bubbles. Marxen & Henningson (2011) note that, contrary to short separation bubbles, vortex roll-up in long bubbles occurs further downstream of the transition location. Under certain conditions, involving minor flow variations, a short separation bubble may significantly elongate, a dynamic process termed "bursting" which has been associated with aerofoil stall by Sandham (2008). It should be noted, however, that bursting and elongation do not necessarily imply that the LSB acquires long bubble characteristics. Although determining appropriate criteria for bubble bursting has been a recurrent topic (Gaster 1967; Diwan & Ramesh 2009; Marxen & Henningson 2011; Serna & Lázaro 2015), the development of a universal criterion has proven difficult, mainly due to the lack of sufficient understanding of the bursting process.

In an effort to characterise short and long bubbles, Gaster (1967) initiated bursting by reducing the wind-tunnel speed, affecting pressure gradient and free stream turbulence. Following a different approach, Marxen & Henningson (2011) induced bursting by eliminating or attenuating disturbances in their DNS boundary conditions. Both studies, therefore, relied on artificial reduction of the amplitude of disturbances in the separated shear layer. It must be noted here, that although this approach is technically straightforward in experimental and numerical frameworks, it does not correspond fully

to the physical sequence of events preceding bubble bursting. The reason is the inability of these approaches to decouple the effect of local mean flow stability changes (i.e. mean flow deformation) and the effect of incoming perturbation amplitude, since the latter is varied. Nevertheless, based on these studies, a hypothesis can be formulated regarding global changes of the size of LSBs as a function of incoming disturbances which could lay the foundation for elucidating both the flapping and bursting mechanisms (Marxen & Henningson 2011). Namely, the amplitude of flow perturbations entering the LSB defines the breakdown location which, in turn, defines the size of the LSB and the growth of the developing instabilities. The evaluation of such a hypothesis in an experimental framework is the premise of the present study, in reference to the numerical study of Marxen & Henningson (2011).

This work investigates the response of laminar separation bubbles to impulsive forcing by assessing the attendant changes of flow dynamics and the underlying stability mechanism. Through the above, further insight is provided into both flapping and bursting mechanisms. A laminar separation bubble is induced on a flat plate by an externally imposed adverse pressure gradient. Based on the maximum reverse flow criterion, the formed LSB is globally stable but convectively unstable (Gaster 1992; Alam & Sandham 2000). Repetitive, two-dimensional, impulsive disturbances are introduced upstream of the location of LSB separation point by means of a dielectric barrier discharge (DBD) plasma actuator (Corke et al. 2010; Kotsonis 2015; Yarusevych & Kotsonis 2017). The premise of using impulsive, spanwise uniform, disturbances is twofold. Firstly, impulsive excitation features a broad spectral content, giving rise to the naturally pertinent instability modes through selective amplification. Secondly, for constant conditions (freestream velocity and turbulence levels) the inflow of the LSB experiences an elevated incoming disturbance amplitude only during the short duration of the impulse. At all other instants, the LSB experiences a natural level of incoming disturbances. Effectively, this enables monitoring mean flow deformation effects, following the wave packet convection, without altering the amplitude of incoming disturbances.

The evolution of the emerging wave packet and the response of the LSB are captured with time-resolved particle image velocimetry (PIV), demonstrating that bursting occurs shortly after the convection of the wave packet. Finally, linear stability theory is employed in order to relate pertinent changes in stability characteristics to the changes in LSB dynamics. Since the aforementioned studies (Häggmark et al. 2001; Rist & Maucher 2002; Marxen & Rist 2010) involving linear stability theory analysis only consider stability characteristics of the mean flow, a necessity rises of investigating dynamic stability, for which quasi-steady assumptions may be made. LST in the spatial formulation is, therefore, applied on phase-averaged velocity fields within a forcing cycle in order to assess changes in stability characteristics from bursting until recovery of the LSB to its unperturbed state.

2. Experimental apparatus and techniques

2.1. Model set-up

Experiments are carried out in an open-loop wind tunnel with square cross-section of 500mm×500mm. An overview of the experimental setup is shown in figure 1. A 20mm thick, 500mm wide and 1000mm long Plexiglas[®] flat plate is inserted in the test section off-centre at a 30% distance from the floor for alleviating wind tunnel corner effects (Saric & White 1998). The flat plate leading edge is a modified super ellipse (Lin *et al.* 1992), enabling seamless curvature change and ensuring development of laminar boundary layer.

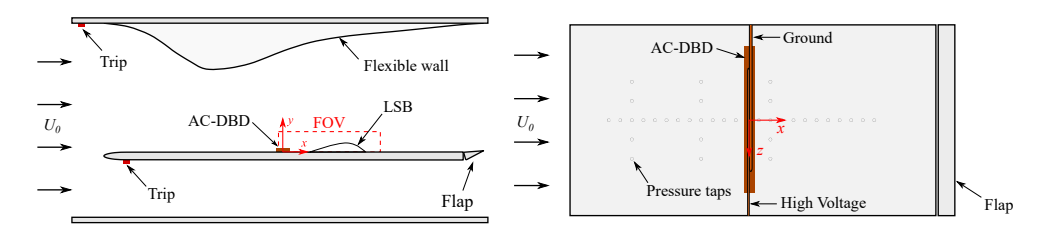


FIGURE 1. Schematic of the experimental setup.

A movable flap is positioned at the trailing edge of the flat plate and is deflected such as to localise the leading edge stagnation point on the upper side of the flat plate, eliminating possible unsteady separation effects. The pressure gradient on the flat plate surface is conditioned with the aid of a flexible, 1mm thick polycarbonate wall, positioned on the opposite side of the test section. A Cartesian coordinate system is defined such that $\tilde{x}=0$ lies 420mm from the leading edge of the flat plate, $\tilde{y}=0$ at its top surface and $\tilde{z}=0$ at its midspan. Here, the tilde denotes dimensional quantities.

The boundary layer on the lower side of the flat plate is tripped at a distance of 50mm from the leading edge by means of a 2mm thick ziz-zag turbulator. This is done for eliminating possible fluctuations of a laminar boundary layer as well as for reducing the strength of shedding at the trailing edge flap. The same tripping technique is applied at the upstream end of the flexible wall in order to avoid unsteady separation in the adverse pressure gradient region. Suppression of these effects was confirmed during preliminary studies by employing both tuft flow visualisation and PIV measurements. In addition, flow field surveys with a stethoscope confirmed that the boundary layer does not relaminarise in the favourable pressure gradient region.

The freestream velocity (U_0) is set using a Pitot-static tube located 100mm upstream of the flat plate leading edge and is kept constant at 6.4m/s, with uncertainty lower than 2%. Hot-wire measurements, bandpass filtered between 0.1Hz and 1kHz, were used to estimate freestream turbulence intensity (TI = $\tilde{U}'_{\rm rms}/\tilde{U}_0$), determined to be under 0.2%.

The pressure distribution imposed by the flexible wall is measured by means of 36 pressure taps integrated in the flat plate (figure 1) and is expressed in terms of surface pressure coefficient (C_p) . In the streamwise direction, pressure taps are located at the midspan ($\tilde{z}=0$) with 30mm spacing. Spanwise taps are spaced symmetrically with respect to the midspan at three streamwise locations; $\tilde{x} = -260 \,\mathrm{mm}$, $-80 \,\mathrm{mm}$ and $100 \,\mathrm{mm}$, with a spanwise spacing of 50mm. Measurements are performed with a high accuracy multi-channel pressure scanner at an acquisition frequency of 10Hz and mean pressures are estimated from 150 samples at each location. The obtained mean C_p distribution is shown in figure 2. The presence of a pressure plateau in the streamwise surface pressure distribution (figure 2a) indicates the formation of a laminar separation bubble (e.g. Yarusevych et al. 2009) in the interval between $\tilde{x} \approx 30 \text{mm}$ and $\tilde{x} \approx 150 \text{mm}$. The presence of a laminar separation bubble is confirmed by tripping the boundary layer with a zigzag turbulator placed at the leading edge of the flat plate. The resulting streamwise pressure distribution (figure 2a) shows that the turbulent boundary layer overcomes the adverse pressure gradient without separating and that C_p increases downstream without exhibiting the typical for laminar separation bubbles pressure plateau. Figure 2b demonstrates that both clean and tripped configurations produce uniform pressure distribution in the spanwise direction, ensuring essentially two-dimensional conditions in the time averaged sense.

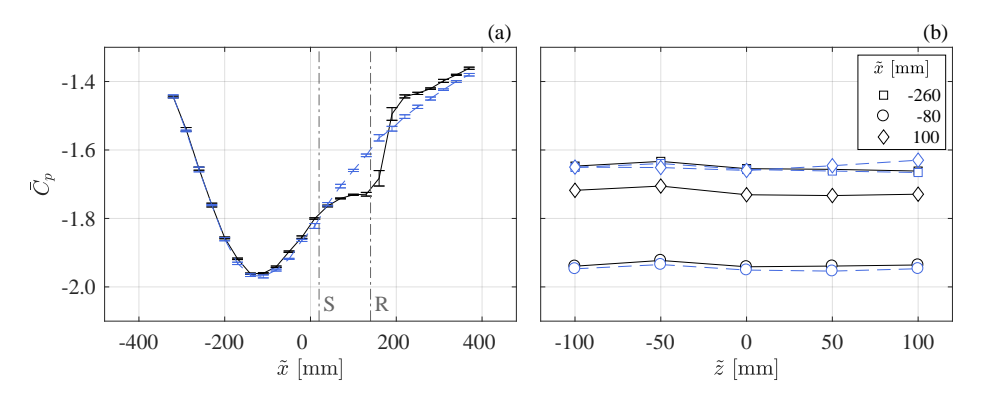


FIGURE 2. C_p distribution in (a) streamwise direction ($\tilde{z} = 0$) and (b) spanwise direction. Solid lines: clean flat plate conditions; dashed lines: tripped boundary layer near the leading edge.

2.2. AC-DBD forcing

Controlled disturbances are introduced upstream of the LSB with the use of an Alternating Current Dielectric Barrier Discharge (AC-DBD) plasma actuator (Corke et al. 2010; Benard & Moreau 2014; Kotsonis 2015; Yarusevych & Kotsonis 2017), located just upstream of the mean separation point (figure 1). It consists of two asymmetrically positioned electrodes, separated by a dielectric layer. When activated, the DBD plasma actuator enables momentum exchange through ion-neutral collisions resulting in the formation of a wall-parallel jet near the surface (Kotsonis 2015). Deterministic perturbations in terms of amplitude and frequency can, therefore, be introduced by manipulating the carrier signal. Being an electric device, the DBD plasma actuator has a fast response and precisely controlled frequency and amplitude. For this study, the streamwise extent of the high voltage and ground electrodes are 2mm and 5mm respectively. Both electrodes are painted on the surfaces using conductive silver coating and are less than $10\mu m$ in thickness. The dielectric comprises of $60\mu m$ thick $Kapton^{(8)}$ polyimide film, however, its thickness is significantly lower than the local boundary layer displacement thickness (≈ 5.5 mm). Preliminary studies have confirmed negligible influence on the bubble dynamics from the mechanical roughness associated with the actuator. The discharge gap is located at a distance of 420mm from the leading edge and serves as the origin of the reference system (figure 1).

The actuator is driven by a digitally controlled high voltage amplifier. The forcing signal is comprised by repetitive pulses as shown in figure 3. Each pulse is constructed by modulating the sinusoidal carrier signal ($\tilde{f}_c = 5 \text{kHz}$) with a square signal at significantly lower pulse frequency of $\tilde{f}_p = 2 \text{Hz}$. The duty cycle of modulation is fixed at 0.2%, resulting in a pulse width of 1ms. As will be shown in a later section, the relevant hydrodynamic frequency associated with the primary shear layer instability in the current LSB is 136Hz. Respectively, the frequency associated with flapping is on the order of 10 Hz. With the carrier frequency exceeding any relevant hydrodynamic frequency by at least two orders of magnitude, each 1ms burst is essentially equivalent to a single impulsive perturbation. Furthermore, the frequency of the pulses ($\tilde{f}_p = 2 \text{Hz}$) is selected such that the bubble fully recovers to its unperturbed state between two consecutive pulses. Thus, the perturbations introduced represent a sequence of statistically independent impulses, facilitating phase-averaging of the flow measurements.

In order to assess the effect of the excitation amplitude on LSB topology and dynamics, several peak to peak voltage amplitudes are considered, between 2.5kV and 5kV. Charac-

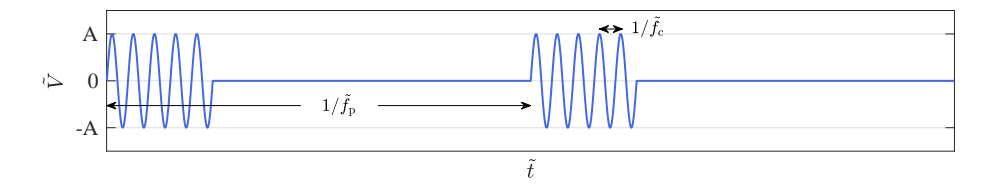


FIGURE 3. Sample of the DBD plasma actuator forcing signal of amplitude A. The sinusoidal signal at carrier frequency $\tilde{f}_c = 5 \text{kHz}$ is modulated with a square wave of pulse frequency $\tilde{f}_p = 2 \text{Hz}$. Duty cycle is 0.2% leading to 1ms pulse width.

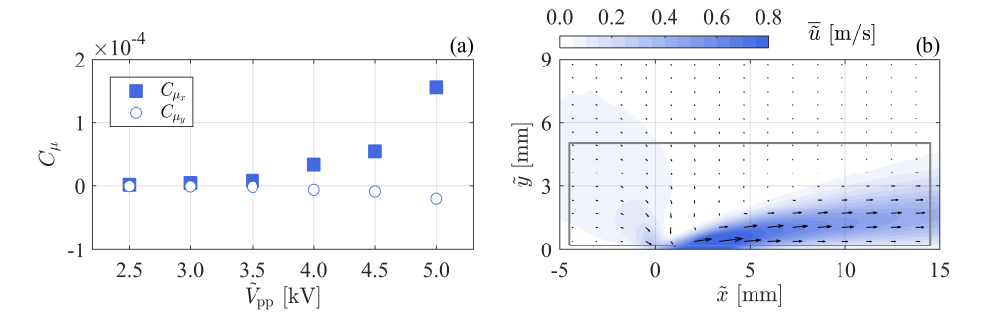


FIGURE 4. (a) DBD plasma actuator momentum coefficient as a function of applied voltage. (b) Time-averaged plasma-induced velocity field in quiescent conditions for $\tilde{V}_{pp} = 5 \text{kV}$. The control volume boundary for the C_{μ} estimation is indicated by a gray rectangle.

terisation of the forcing exerted on the fluid by the AC-DBD for the applied voltages is expressed in terms of momentum coefficient (C_{μ}) , as formulated by Amitay *et al.* (2001).

$$C_{\mu} = \frac{\overline{\tilde{\mathbf{I}}}}{\frac{1}{2}\tilde{\rho}_{0}\tilde{U}_{0}^{2}\tilde{l}} \tag{2.1}$$

Here, the time-averaged momentum per unit length, $\tilde{\mathbf{I}}$, is normalised by the freestream fluid density, $\tilde{\rho}_0$, the square of the freestream velocity, \tilde{U}_0 , and the length of the plasma actuator, \tilde{l} . For estimating $\tilde{\mathbf{I}}$ at each voltage, PIV measurements are carried out in quiescent conditions with the actuator operating continuously at $\tilde{f}_c = 5 \mathrm{kHz}$. $\tilde{\mathbf{I}}$ is then calculated as described by Kotsonis et~al.~(2011) through application of the momentum balance equation,

$$\bar{\tilde{\mathbf{I}}} = \oint_{s} \tilde{\rho}_{0} \ \overline{\tilde{\boldsymbol{u}}} \left(\overline{\tilde{\boldsymbol{u}}} \cdot \hat{\boldsymbol{n}} \right) d\tilde{S}$$
 (2.2)

to the appropriate control volume, assuming uniform pressure distribution. It should be noted here, that the described momentum coefficient is calculated based on continuous operation of the actuator and, as such, pertains to the mechanical power of the actuator. Since for the LSB control the actuator is operated in a modulated manner, the momentum transferred to the flow during each individual pulse can be extracted by simply multiplying the relevant momentum coefficient by the duty cycle.

The estimated C_{μ} during continuous operation under quiescent conditions for each applied voltage and an exemplary velocity field are shown in figure 4. Evidently, the largest contribution in forcing originates from the momentum exchange along the x-direction (C_{μ_x}) . As fluid is displaced by the jet, a secondary effect is observed in the region

of the discharge gap ($\tilde{x}=0$). As a result, thrust along the y-direction is generated towards the wall, signified by negative momentum coefficient (C_{μ_y}). Although the magnitude of momentum coefficient is proportional to the voltage, C_{μ_y} remains significantly lower than C_{μ_x} for all applied voltage amplitudes. For the remainder of the study, $C_{\mu} \approx C_{\mu_x}$ will be used as an indicator of actuator strength. Finally, it is important to note, that the topology of the jet as well as the value of C_{μ} are largely unchanged in the case of the relatively weak external flow encountered in this study (Pereira et al. 2014).

2.3. Two-component PIV

A time-resolved, two-component Particle Image Velocimetry (PIV) system is employed for investigating the flowfield in the x-y plane as seen in figure 1. Illumination is performed by a laser system that delivers green light (532nm). The beam is transformed into a 1mm light sheet with the aid of an array of spherical and cylindrical lenses. Two high-speed cameras with 1024×1024 pixels sensor resolution are used to image the illuminated region. Both are equipped with 200mm macro objectives set at an aperture of f/5.6. Particle seeding consists of vaporised water-glycol mixture droplets of 1 µm diameter. Acquisition frequencies (f_a) at 250Hz, 500Hz and 2000Hz are selected for obtaining statistics and resolving high frequency phenomena accordingly. For each acquisition frequency, 10914 cropped image pairs ($\Delta t = 60 \mu s$) are recorded, resulting in total acquisition times of 43.7s, 21.8s and 5.5s respectively. The image pairs are acquired and processed with LaVision DaVis 8.3. The magnification factor is M=0.29, yielding a resolution of 14px/mm for each camera. Particle displacements are calculated by applying the multistep interrogation algorithm (Scarano & Riethmuller 2000) from an initial window of 48×48 pixels to a final window of 12×12 pixels with a 75% overlap between windows. The resulting vector spacing is 0.19mm in both x and y directions. The multi-step interrogation window sizes have been selected such that the final vector spacing matches the limit of spatial resolution determined via the method described by Kähler et al. (2012). Vector fields from the two cameras are stitched together to obtain a combined field of view of 131mm by 14mm.

For the experimental data presented in this work, uncertainty is quantified using the correlation statistics method Wieneke (2015). The local error for instantaneous velocity measurements is estimated to be $\varepsilon_u \approx 1\%$ in the free stream and $\varepsilon_u \approx 10\%$ within the LSB. Maximum uncertainty is associated with the region of shear layer breakdown and reattachment. At this location, the uncertainty in the phase-averaged velocity fields is 3%, 5% and 8% for acquisition frequencies of 250Hz, 500Hz and 2000Hz respectively. Since the majority of results discussed in the present study pertain to an acquisition frequency of $\tilde{f}_a = 500$ Hz, the corresponding uncertainty is propagated through the analysis to yield uncertainty estimates for the location of the LSB dividing streamline (< 2.5%) and LST growth rates (< 3.5%).

Actuation and PIV measurements are digitally controlled and synchronised. The reference time $\tilde{t}_0 = 0$ s is set at the moment when the actuator is activated. Subsequently, the camera shutter and laser pulse signals are used for establishing the time of the first measurement to within 1 μ s.

3. Post-processing methodology

3.1. Notation and scaling

Throughout this report, dimensional quantities are noted by a tilde and are accompanied by the respective unit (e.g. \tilde{x} [mm]). For non-dimensional representation, measured

and computed quantities are globally normalised with representative scaling parameters from the baseline unforced LSB. More specifically, all lengths are normalised with the displacement thickness at the separation point of the unforced LSB ($\tilde{\delta}_{s_0}^* = 2.39 \text{mm}$). Integral boundary layer parameters are estimated based on the numerical integration of the measured time-averaged velocity field. Velocities are non-dimensionalised with the local edge velocity at separation, $\tilde{U}_{\infty_s} = 8.6 \text{m/s}$. These two scaling factors are employed for defining the Reynolds number as $Re_{\delta_s^*} = \tilde{U}_{\infty_s} \tilde{\delta}_{s_0}^* / \tilde{\nu} = 1305$. Furthermore, they are combined for frequency scaling in the form of a Strouhal number, $St = \tilde{f} \ \tilde{\delta}_{s_0}^* / \tilde{U}_{\infty_s}$. All non-dimensional quantities are denoted by their respective symbol (e.g. $x = \tilde{x}/\tilde{\delta}_{s_0}^*$, $u = \tilde{u}/\tilde{U}_{\infty_s}$). Time-averaged quantities are identified with an overbar (e.g. \bar{u}), whereas temporal fluctuations are marked by a dash (e.g. u').

An additional scaling scheme is introduced for the comparison of forced and unforced cases. Accordingly, quantities are scaled with the respective time-averaged value pertaining to the unforced LSB for each case. For example, the separation point, x_s , is scaled with the mean separation point of the unforced LSB, \bar{x}_{s_0} . All scaled primary (e.g. length) and derived (e.g. vorticity) quantities, are subsequently denoted by a hat (e.g. $\hat{x} = x/\bar{x}_{s_0}$, $\hat{\omega} = \omega/\bar{\omega}_{s_0}$).

As mentioned in section 2.2, the LSB is cyclically forced by pulses of frequency $\tilde{f}_{\rm p} = 2$ Hz. Therefore, a non-dimensional phase, ϕ , is defined based on the pulse frequency and the time interval elapsed from the preceding pulse, \tilde{t} (equation 3.1).

$$\phi = \tilde{t}\tilde{f}_{\mathbf{p}} \tag{3.1}$$

Consequently, $\phi = 0$ coincides with the moment of actuation, while $\phi = 1$ occurs after a time interval of $\tilde{t} = 1/\tilde{f}_{\rm p}$, at the moment prior to the next pulse initiation. Phase-averaged quantities are denoted with chevron brackets (e.g. $\langle u \rangle$).

3.2. Linear Stability Theory

Similarly to earlier studies (Häggmark et al. 2001; Rist & Maucher 2002; Jones et al. 2010; Marxen & Rist 2010; Yarusevych & Kotsonis 2017) the stability characteristics of the LSB mean flow field are investigated using linear stability theory (LST). The latter assumes local parallel flow and low amplitude wave-like disturbances. While these assumptions are approximations for separated flows such as the LSB at hand, the above studies have shown very good agreement between LST predictions and direct numerical simulation (DNS) or experimental data. In classical LST analysis (e.g. van Ingen 2008), the amplification of disturbances is governed by the Orr-Sommerfeld eigenvalue problem,

$$(D_y^2 - \alpha^2 - \beta^2)^2 \varphi(y) = iRe \left[(\alpha \bar{u} + \beta \bar{w} - \omega)(D_y^2 - \alpha^2 - \beta^2) - \alpha D_y^2 \bar{u} - \beta D_y^2 \bar{w} \right] \varphi(y)$$
(3.2)

Here, α and β are the complex streamwise and spanwise wavenumbers respectively while ω is the corresponding wave frequency. The problem is solved in spatial formulation, i.e. for real values of ω . A detailed description of the solution process may be found in the work of van Ingen & Kotsonis (2011). For this study, two-dimensional flow is assumed and only streamwise disturbances are considered, therefore, $\beta=0$ and $\bar{w}=0$.

The amplification factor, N, is expressed by equation 3.3,

$$N = \ln\left(\frac{\tilde{A}}{\tilde{A}_0}\right) = \int_{\tilde{x}_c}^{\tilde{x}} -\tilde{\alpha}_i d\tilde{x}$$
 (3.3)

with \tilde{x}_c being the critical streamwise location where a disturbance of amplitude \tilde{A}_0 and frequency ω first becomes unstable. Due to practical limitations of experimental techniques, it is not possible to directly measure minute amplitude of disturbances prior to their amplification above a given measurement noise level. This renders experimental determination of the critical point difficult. However, in the upstream part of the LSB, α_i may be approximated by a second order polynomial (e.g. Jones *et al.* 2010, cf. figure 11). As a result, it is possible to estimate x_c by extrapolating the fit curve to $\alpha_i = 0$. Using this approach, the N factor at the beginning of the imaged field of view is quantified and serves as a constant for the integration thereon.

Linear stability in temporally variable baseline flows may generally be treated following the formulation of Reynolds & Hussain (1972). The latter differs from the classical Orr-Sommerfeld eigenvalue problem, by the inclusion of Reynolds stress terms. It is well asserted that global flow modification in the region of the LSB is associated with rather low frequencies, e.g. changes experienced due to flapping or bursting (Gaster 1967; Marxen & Henningson 2011). In contrast, the objective of LST is to describe the growth of instabilities of significantly higher frequencies, such as the pertinent Kelvin-Helmholtz modes developing in the separated shear layer. Due to this large timescale separation, LST modes essentially experience a quasi-steady baseline flow at a given time after the introduction of a pulse. Further discussion on the timescale separation is carried out in section 5.2. A quasi-steady assumption can, therefore, be made and LST calculations may be performed on phase-averaged velocity profiles, omitting Reynolds stress terms, thus arriving to equation 3.2. This approach has been treated and discussed in past studies (e.g. von Kerczek & Davis 1974; Brevdo & Bridges 1997). Finally, it should be stressed that non-linear effects cannot be predicted using LST, especially in the aft part of the LSB, where high amplitude three dimensional structures are dominant (e.g. Alam & Sandham 2000). Reliable stability estimates are, therefore, expected in the fore portion of the bubble, where the amplitude of disturbances is relatively low.

3.3. Proper Orthogonal Decomposition (POD)

Identification of coherent structures and data order reduction are performed via the snapshot POD method suggested by Sirovich (1987). The fluctuations of the velocity field, u', are first decomposed to a set of eigenfunctions, Φ . The latter are sorted in decreasing order of eigenvalue (λ). Hence, eigenfunctions with large eigenvalue represent the most dominant flow structures. A reduced order representation (denoted by the subscript $_{\rm ro}$) may, therefore, be achieved by summation of the time-averaged velocity field and few selected spatial eigenfunctions by means of equation 3.4, where, a are the temporal coefficients, unique to each snapshot.

$$u_{\text{ro}}(x,t) = \bar{u}(x) + \sum_{n=1}^{N_{\text{ro}}} a^{(n)}(t) \Phi^{(n)}(x)$$
 (3.4)

The analysis shows that for both unforced and forced cases studied here, 85% of the total estimated modal energy is concentrated within the first four POD modes (figure 5a). A preliminary study sought in identifying the underlying phenomena that each of the first four modes represent. In the unforced scenario, $\boldsymbol{\Phi}^{(1)}$ captures fluctuations of the shear layer attributed to the flapping behaviour. The following eigenfunctions, $\boldsymbol{\Phi}^{(2)}$ and $\boldsymbol{\Phi}^{(3)}$ represent the convective shedding of the LSB. Similar observations regarding the first three modes have been made by Lengani *et al.* (2014). When the bubble is forced (figure 5b-5e), $\boldsymbol{\Phi}^{(1)}$ remains to be associated with the shear layer flapping while the second eigenfunction, $\boldsymbol{\Phi}^{(2)}$ represents the rapid shrinkage and recovery of the LSB shear

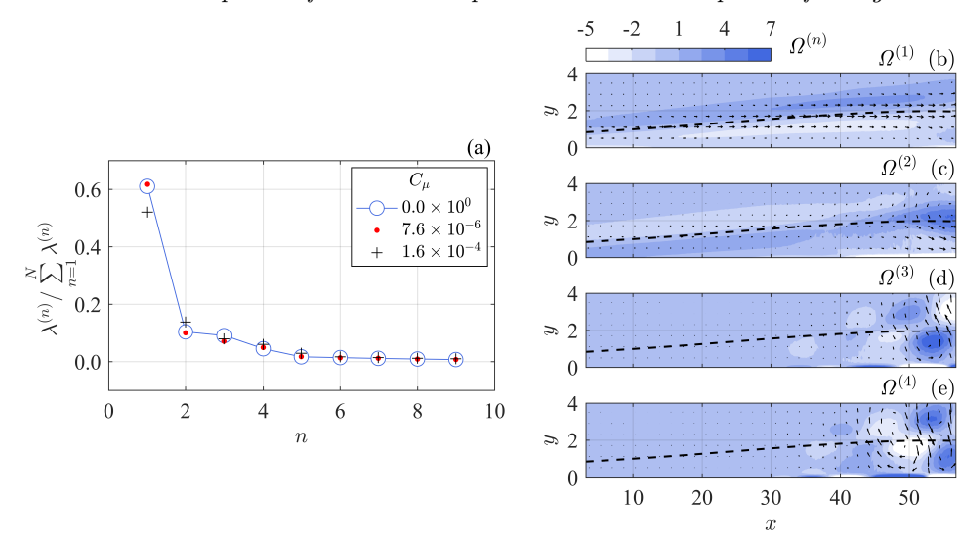


FIGURE 5. (a) Nine first POD eigenvalues for unforced and forced LSB. (b)-(e) Curl between the streamwise and wall-normal component of the first four eigenfunctions, $\Omega^{(n)} = \nabla \times (\Phi_u^{(n)}, \Phi_v^{(n)})$ for $C_{\mu} = 1.6 \times 10^{-4}$. Dashed line: displacement thickness.

layer that is later described in section 5.1. Shedding and convection of the introduced disturbance are simultaneously captured in $\Phi^{(3)}$ and $\Phi^{(4)}$, as they assume the same frequency.

3.4. Wavelet analysis

An in-depth overview of wavelet analysis may be found in the work of Daubechies (1992), thus, only the essential concepts are hereby mentioned. In contrast to the discrete Fourier transform, the wavelet transform is suitable for capturing the spectral content of an arbitrary temporal signal, $\tilde{u}(\tilde{t})$, such as the impulsive disturbance pertinent to this study. First, a baseline wavelet function, ψ , must be chosen having zero mean and being localised in both time and frequency space. For this study, the Morlet wavelet is selected (equation 3.5).

$$\psi = e^{-(\tilde{t}/\tilde{c})^2} e^{i2\pi \tilde{f}_c \tilde{t}} \tag{3.5}$$

In order to satisfy the wavelet admissibility condition described by Farge (1992), the wavelet central angular frequency is selected to be $2\pi \tilde{f}_c = 5 \text{rad/s}$ while the damping parameter is $\tilde{c} = 2 \text{s}$.

Wavelet coefficients, w, can then be estimated via expression 3.6, which represents the convolution between the examined temporal signal, $\tilde{u}(\tilde{t})$, and the translated and dilated complex conjugate of ψ , denoted as ψ^* .

$$w = \frac{\tilde{s}^{-1/2}}{\sqrt{2\pi\tilde{f}_{\rm a}}} \int_{-\infty}^{\infty} \psi^* \left(\frac{\tilde{t} - \tilde{\tau}}{\tilde{s}}\right) \tilde{u}(\tilde{t}) d\tilde{t}$$
 (3.6)

Here, translation and dilation scales of ψ are represented by the terms τ and s respectively. In order to obtain unit power per scale, w is scaled by $\sqrt{2\pi \tilde{f}_{\rm a}}$, with $\tilde{f}_{\rm a}$ being the temporal signal sampling frequency.

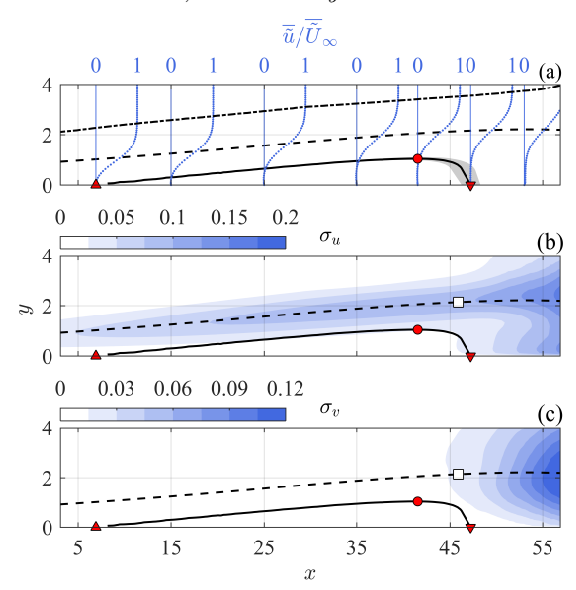


FIGURE 6. Unforced LSB. (a) Time-averaged streamwise velocity profiles, scaled with the local freestream velocity. (b) Streamwise velocity fluctuations. (c) Wall-normal velocity fluctuations. Solid line: dividing streamline, dashed line: displacement thickness, dash-dotted line: $\delta_{99\%}$. \triangle : separation point, ∇ : reattachment point, \circ : maximum height, \square : maximum shape factor. Shaded region: dividing streamline uncertainty limits for $\tilde{f}_a = 500$ Hz (see section 2.3).

4. The unforced LSB

4.1. Statistical features

Prior to the analysis of the spatio-temporal response of the bubble to the impulsive forcing, it is instructive to examine the behaviour pertaining to the natural, unforced flow, serving as baseline in this study. Figure 6 depicts time-averaged and fluctuating fields of the unforced flow. Driven by the adverse pressure gradient, the flow separates and reattaches downstream forming a closed, in the time-averaged sense, laminar separation bubble. The boundary of the LSB is defined by the mean dividing streamline, where the streamfunction $\psi=0$. The mean separation and reattachment points are estimated at $\bar{x}_{\rm s}=6.3$ and $\bar{x}_{\rm r}=47.5$, establishing a bubble length of $\bar{l}_{\rm b}=41.2$. The height of the bubble is defined as the point of the dividing streamline that is most distant from the wall, $\bar{h}=0.73$, and is located at $\bar{x}_{\rm h}=41.7$. The maximum reverse flow observed within the bubble is on the order of 2% of the local freestream velocity, indicating development of only convective instabilities as suggested by Gaster (1992), Alam & Sandham (2000) and Rist & Maucher (2002).

Time-averaged streamwise velocity profiles scaled with the local freestream velocity (\tilde{U}_{∞}) are provided for several streamwise stations in figure 6a. These profiles are similar to the hyperbolic tangent approximations suggested by Dovgal *et al.* (1994) as well as with hot-wire measured profiles rectified in proximity to the wall (Niew 1993; Watmuff 1999; Diwan & Ramesh 2009). Similar to the studies of Gaster & Grant (1975) and Marxen & Henningson (2011), reattachment is turbulent, however, there is no correspondence with a fully developed turbulent velocity profile (log-law) in the downstream vicinity of the reattachment. Indeed, as Alam & Sandham (2000) indicate, relaxation of the boundary layer to a fully turbulent equilibrium state may require several bubble lengths, well downstream of the current field of view.

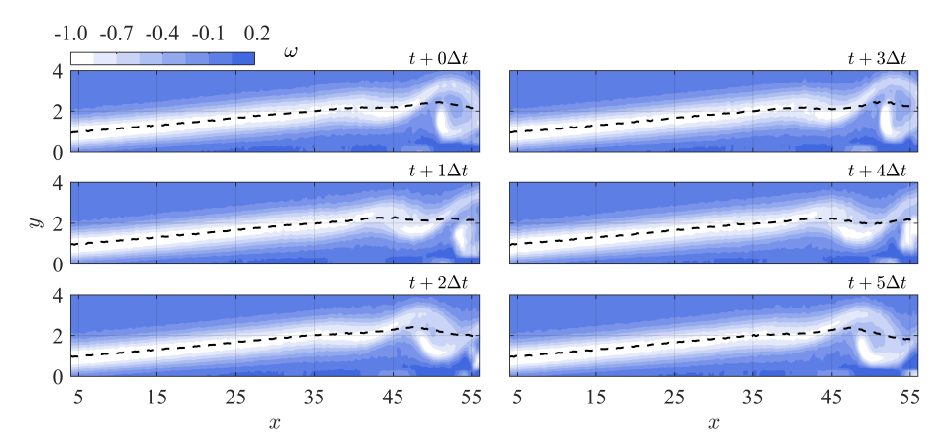


FIGURE 7. Instantaneous vorticity demonstrating coherent vortex shedding at timesteps separated by $\Delta t = 5\tilde{f}_{\rm p}/\tilde{f}_{\rm a}$, with $\tilde{f}_{\rm a} = 2 {\rm kHz}$. Dashed line: displacement thickness (δ^*).

Fluctuations in the velocity field are quantified by the standard deviation of the two velocity components, $\sigma_u = \tilde{\sigma}_u/U_0$ and $\sigma_v = \tilde{\sigma}_v/U_0$ (figures 6b and 6c). Two regions of increased fluctuation can be identified, the first extending along the displacement thickness, upstream of \bar{x}_h . In this region, small variations in the shear layer distance from the wall due to the flapping mechanism (Zaman et al. 1989) result in substantial changes in the value of u. Flapping does not affect the wall-normal velocity to the same extent, thus this region is absent in the σ_v field. In contrast, the second region of elevated fluctuations is evident in both standard deviation fields downstream of \bar{x}_h . Here, fluctuations are attributed to coherent vortex shedding (figure 7) and the subsequent breakdown to turbulence. In both velocity components, the associated velocity fluctuations are concentrated about the displacement thickness, known to approximate the trajectory of the shed structures (e.g. Boutilier & Yarusevych 2012).

4.2. Spectral content and stability characteristics

The global displacement of the separated shear layer in a LSB, i.e. flapping, is known to occur at significantly lower frequencies than the respective vortex rollup and shedding (e.g. Hain et al. 2009). To access the spectral content of the shear layer flapping and vortex shedding of the unforced LSB, velocity measurements are performed at $f_{\rm a}=250{\rm Hz}$ and $f_a = 2000$ Hz respectively. The selection of reference locations is made based on results in figure 6. For assessing flapping, a temporal signal, u(t) is extracted at the streamwise location corresponding to the mean separation point, $\bar{x}_{\rm s}$, and at wall normal location corresponding to $\delta^*(\bar{x}_s)$. Here, minimal vortex shedding signature is expected in the spectra. For characterising vortex shedding in the aft part of the bubble, a v(t)signal is sampled at the streamwise location of mean maximum height and wall-normal distance equal to the displacement thickness $\delta^*(\bar{x}_h)$. Power spectral density is estimated via the Welch method (Welch 1967) by dividing the corresponding temporal signal into 6 windows with 50% overlap. The resulting frequency resolution is $St = 3.6 \times 10^{-5}$ and 2.8×10^{-4} (0.13Hz and 0.98Hz) for each of the two acquisition frequencies, respectively. The results shown in figure 8a suggest that flapping is comprised of a range of frequencies below St = 0.005 (18Hz). The two peaks present in the vicinity of $St \approx 0.005$ are attributed to aliasing from shedding signature and are approximately three orders of magnitude weaker than the highest point in the band. In contrast, shedding in the aft

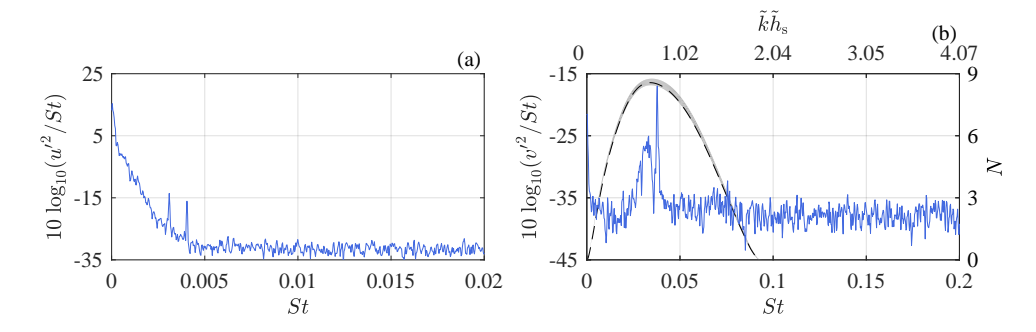


FIGURE 8. Power spectral density of the unforced LSB. (a) u(t) at $x = \bar{x}_s$ and $y = \delta^*(\bar{x}_s)$, $\tilde{f}_a = 250$ Hz. (b) v(t) at $x = \bar{x}_h$ and $y = \delta^*(\bar{x}_h)$, $\tilde{f}_a = 2000$ Hz. Dashed line: N factor at the same location. Shaded region: N factor uncertainty at $\tilde{f}_a = 500$ Hz (see section 2.3).

portion of the bubble produces a well defined, elevated spectral content situated between St=0.022 (80Hz) and St=0.047 (170Hz) (figure 8b). The most dominant frequency is St=0.038 (136Hz), with an order of magnitude higher spectral density than the rest of the band. The spectral content is also related to the dimensionless shedding parameter, $\tilde{k}\tilde{h}_{\rm s}$ (Yang & Voke 2001). Here, $\tilde{k}=2\pi\tilde{f}/\tilde{u}_{\rm infl}$, is the angular wave number, with $\tilde{u}_{\rm infl}$ being the inflection point velocity at $\bar{x}_{\rm h}$, and $\tilde{h}_{\rm s}$ is the shear layer thickness, equal to the displacement thickness at the same location. For the dominant shedding frequency, $\tilde{k}\tilde{h}_{\rm s}=0.78$, lying well within the expected limits for Kelvin-Helmholtz instability (0 < $\tilde{k}\tilde{h}_{\rm s}<1.2785$, Yang & Voke 2001). Furthermore, this is in good agreement with other relevant studies, e.g. Häggmark et al. (2001) and Simoni et al. (2012b).

In addition to spectral measurements, LST analysis is instrumental for identifying the dynamic characteristics relevant to the growth of instabilities in the separated shear layer. For validation purposes, a comparison between spectral results and N factors computed from LST analysis is shown in figure 8b. It can be seen that the frequencies associated with maximum amplification factor are in excellent agreement with that of the dominant peak in the spectrum, both corresponding to St=0.038 (136Hz). The results of linear stability calculations (section 3.2) performed on the time-averaged streamwise velocity field (figure 6a) are presented in figure 9a. It is evident that the growth rate of the most unstable frequency wave increases from St=0.033 (117Hz) in the vicinity of separation to a maximum St=0.043 (155Hz) near the mean maximum height (x=42.3). The corresponding amplification factor at this streamwise location is N=7.2, comparable to the direct numerical simulations of Marxen $et\ al.\ (2009)$. Moreover, LST calculations yield a convective speed of disturbances in the unforced LSB of approximately $0.45\tilde{U}_0$. This is in good agreement with observations on the propagation of coherent vortex shedding structures (figure 7).

Monkewitz & Huerre (1982) suggested a scaling scheme for determining the occurrence of Kelvin-Helmholtz instability in free shear layers. Shear layers are characterised by an external and an internal velocity, $U_{\rm e}$ and $U_{\rm i}$, respectively. Their difference, $\Delta U = U_{\rm e} - U_{\rm i}$, is used for calculating the vorticity thickness, $\delta_{\rm w} = \Delta U/(\partial \bar{u}/\partial y)_{\rm max}$. By including the dimensional frequency, \tilde{f} , and the average of the bounding velocities, $\bar{U} = (U_{\rm e} + U_{\rm i})/2$, a dimensionless frequency is expressed as $\omega^* = 0.25\delta_{\rm w}(2\pi\tilde{f})/\bar{U}$. Monkewitz & Huerre (1982) demonstrated that the range of frequencies for Kelvin-Helmholtz instability lies in the interval $0.21 < \omega^* < 0.222$. For the case of laminar separation bubbles, the internal velocity may be assumed negligible ($U_{\rm i} \approx 0$) while the external velocity is equal to the local freestream ($U_{\rm i} \approx U_{\infty}$). Since the distance of the bubble shear layer from the wall

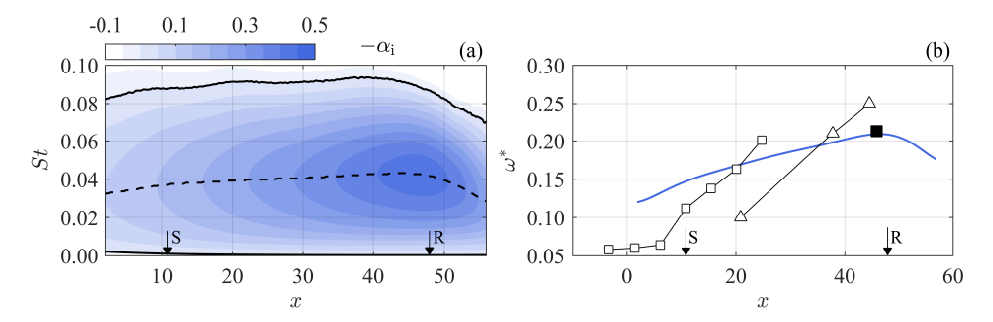


FIGURE 9. Unforced LSB stability diagram. (a) Non-dimensional growth rate, $-\alpha_i = -\tilde{\alpha}_i\tilde{\delta}^*$. Solid line: Neutral curve $(\alpha_i = 0)$. Dashed line: $St(\max\{-\alpha_i\})$ (b) Dimensionless frequency $\omega^* = 0.25\delta_{\rm w}(2\pi\tilde{f})/\bar{U}$. Solid line: ω^* estimated on the most unstable LST frequency. \blacksquare : ω^* with \tilde{f} derived from experimental velocity spectra at the maximum δ^* . \triangle : ω^* from Watmuff (1999); \square : ω^* from Diwan & Ramesh (2009). For comparing datasets, their x axis is scaled such that separation and reattachment locations match with the current experiment.

varies with respect to streamwise position, the aforementioned scaling is not valid unless the shear layer is at sufficient distance from the wall. Consequently, correspondence with the expected range ($\omega^* \approx 0.21$) is mainly achieved in the region of the mean maximum height (e.g Pauley et al. 1990; Watmuff 1999; Simoni et al. 2012a). Figure 9b depicts a comparison between ω^* from the present results and the reporting of Watmuff (1999) and Diwan & Ramesh (2009). The solid line corresponding to ω^* estimated based on the local most unstable frequency (dashed line in figure 9a). Its maximum ($\omega^* = 0.213$), agrees well with the estimate based on the dominant frequency in velocity spectra at the maximum δ^* ($\omega^* = 0.209$). Similar to the aforementioned references, ω^* exhibits linear increase downstream the separation point, confirming the inviscid nature of disturbance amplification (Watmuff 1999). The differences between the slopes of the linear portions of the three data sets are attributed to the substantially different bubble height to length ratio between the respective experiments.

5. The forced LSB

The LSB is subjected to impulsive forcing with amplitudes ranging from $C_{\mu}=1.5\times 10^{-6}$ to $C_{\mu}=1.6\times 10^{-4}$. The pulses are repeated at a frequency of $\tilde{f}_{\rm p}=2{\rm Hz}$. Sample temporal and phase-averaged streamwise velocity signals at the mean maximum height of the unforced LSB are provided in figure 10. The beginning of each cycle is marked by introduction of a pulse and is identified as the vertical grid line. The results illustrate the dynamic nature of the cycle, confirming that the transient completely subsides before the introduction of the next impulse. The strong cycle-to-cycle periodicity affirms the feasibility of phase-averaging for subsequent increase of statistical significance. Experimental limitations dictate that, for each acquisition frequency (250Hz, 500Hz and 2000Hz), the number of realisations available at each phase is 87, 43 and 10, respectively.

5.1. Temporal response to impulse

The pertinent features of the temporal response of the LSB to the impulsive forcing are captured by phase-averaged vorticity fields, $\langle \omega \rangle = \langle \tilde{\omega} \rangle \tilde{\delta}_{s_0}^* / \tilde{U}_0$, shown in figure 11. An animated sequence of the ensuing events is provided as supplementary material. The forcing magnitude of the demonstrated sequence is $C_{\mu} = 5.4 \times 10^{-5}$, though the same general behaviour has been observed at all other forcing amplitudes. An overview of the

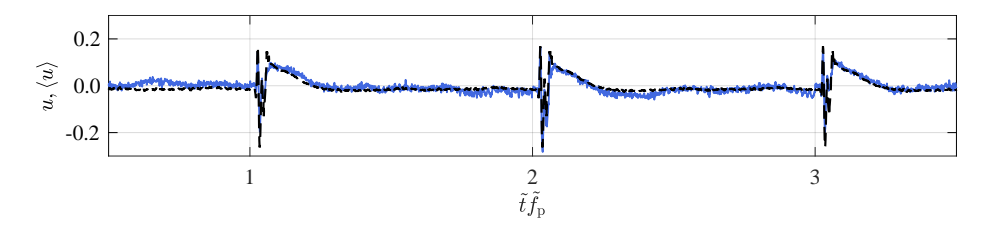


FIGURE 10. Sample of velocity signal at the location of maximum height, \bar{h} , for $C_{\mu} = 1.6 \times 10^{-4}$. The initiation of each forcing cycle is marked by the vertical grid lines. Solid line: raw velocity signal, u. Dashed line: phase-averaged velocity signal, $\langle u \rangle$.

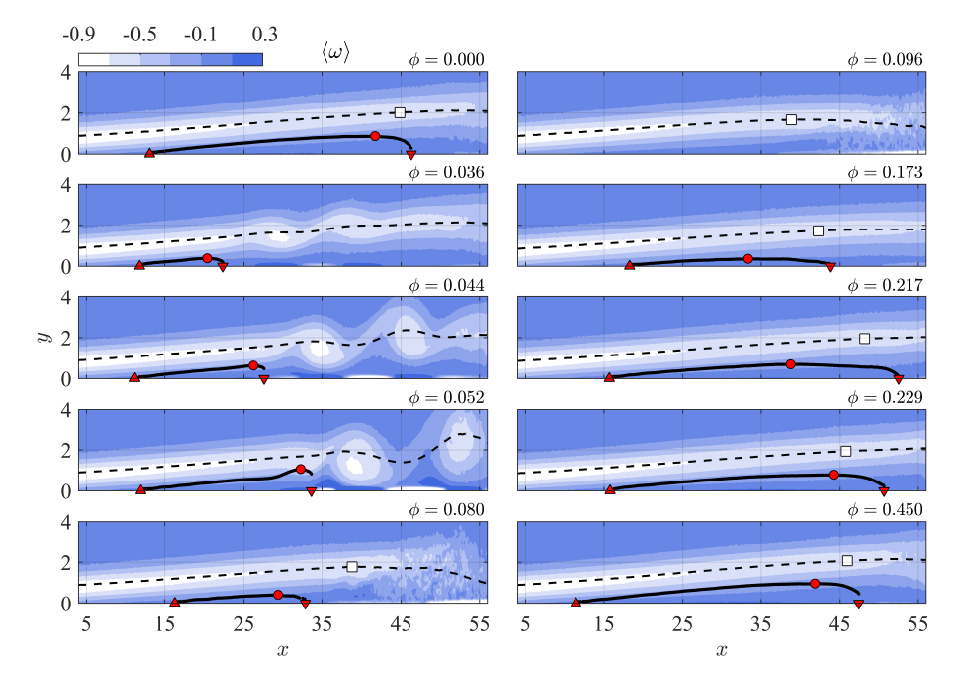


FIGURE 11. Phase-averaged vorticity within the forcing cycle for $C_{\mu} = 5.4 \times 10^{-5}$. Solid line: dividing streamline; dashed line: displacement thickness (δ^*) ; Δ : separation point; ∇ : reattachment point; \circ : maximum height; \square : location of maximum shape factor.

topological changes of the separation bubble for all forcing amplitudes is achieved by tracing bounding properties of the LSB with respect to phase and is shown in figure 12. Specifically, the phase-averaged location of separation, $\langle x_s \rangle$ and reattachment, $\langle x_r \rangle$, bubble length, $\langle l \rangle = \langle x_r \rangle - \langle x_s \rangle$, and maximum height, $\langle h \rangle$ are shown in figure 12. For ease of comparison, these metrics are normalised by the corresponding parameters of the unforced LSB (thus are denoted with the hat symbol). At this point a note needs to be made considering the definition of the LSB boundaries. As seen in figure 11, for phases $\phi < 0.08$, the introduced vortical wavepacket distorts the flow to a degree where a classical definition of LSB is no longer applicable. As such, the focus of the analysis is directed to phases greater than 0.08. In figure 12, the shaded area corresponds indeed to phases at which the introduced disturbance advances within the field of view.

Shortly after the introduction of the pulse, a wave packet emerges, which develops into a set of co-rotating vortices that propagate downstream (0.036 $< \phi < 0.052$, figure 11). The

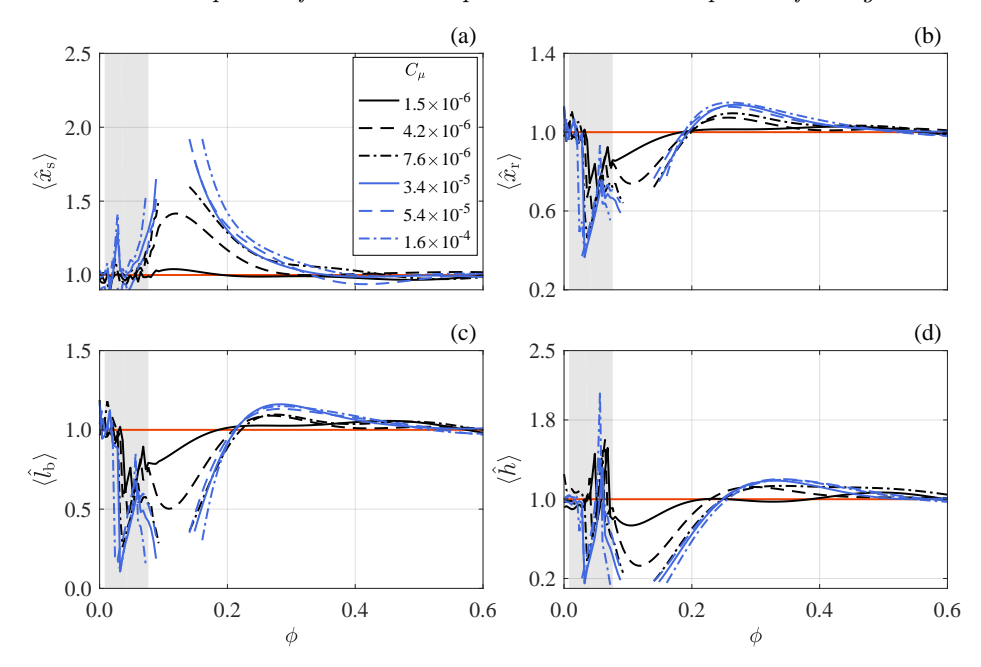


FIGURE 12. Evolution of phase-averaged (a) separation point; (b) reattachment point; (c) bubble length and; (d) maximum bubble height. All metrics are scaled with the respective unforced value. *Shaded region:* Interval during which the wave packet is within the field of view.

convective nature of the developing disturbance confirms the aforementioned assumption of global stability of the present LSB, based on the magnitude of maximum reverse flow of 2% (Gaster 1992; Alam & Sandham 2000). Once the developing wave packet convects past the streamwise location of the mean maximum height of the unforced case ($\phi = 0.08$), the LSB undergoes rapid contraction with the separation and reattachment points shifting downstream and upstream respectively, similar to the DNS observations of Rist & Maucher (2002). For forcing amplitudes exceeding $C_{\mu} = 4.2 \times 10^{-6}$, the LSB is completely eliminated ($\phi = 0.096$, figure 11). Complete elimination of the LSB is signified in figure 12 by discontinuities in the plots at phases close to $\phi = 0.1$. Within the same range, the two lowest forcing amplitudes result in the reduction of LSB size, albeit not complete elimination. From this point, the LSB starts recovering, a process that is significantly slower than the contraction. Growth of the LSB is, too, occurring towards both upstream and downstream directions (figure 12).

During the recovery stage, the LSB elongates before contracting to its unperturbed state ($\phi \approx 0.45$, figure 11). The reattachment point shifts downstream, similar to the behaviour of the bursting process described by Gaster (1967) and Marxen & Henningson (2011). This produces the overshoot in the reattachment location, bubble length, and the maximum height seen in figures 12b, c, and d, respectively, within $0.2 < \phi < 0.4$. Bursting is accompanied by reduction of the vortex shedding strength. This is visualised in figure 13, which depicts instantaneous velocity traces probed at the aft part of the bubble. At the early stages of the bursting process, for a short time interval after the bubble elimination, no shedding traces are evident within the field of view $(0.1 < \tilde{t}\tilde{f} < 0.15)$. Shedding, however, quickly resumes as the bubble grows, albeit at a lower strength, until reattachment assumes its most downstream location ($\phi \approx 0.25$, figure 11). From this point, the bubble height increases further than its unforced value, an inertial effect that

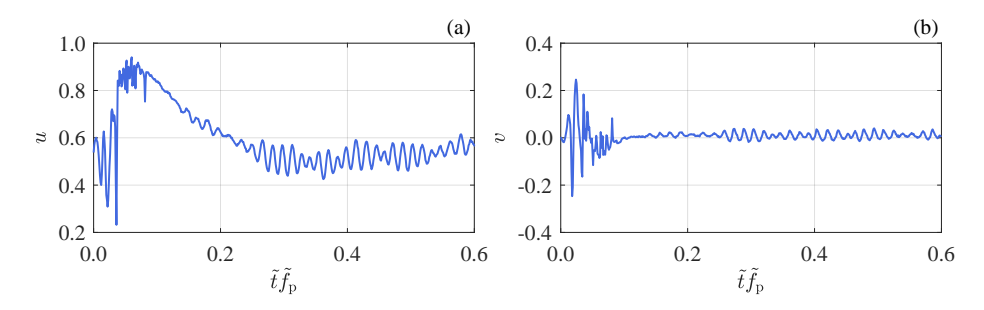


FIGURE 13. Velocity signals at x=55 and $y=\bar{\delta}_0^*(55)$ for $C_{\mu}=5.4\times 10^{-5}$. (a) streamwise component, u. (b) wall-normal component, v.

is a direct consequence of the vortex shedding strength reduction. More specifically, mass accumulation caused by the reverse flow is not balanced by sufficient mass entrainment in the aft portion through vortex shedding until breakdown has moved sufficiently upstream. After the latter occurs, the LSB finally recovers to its unperturbed state.

The dynamic cycle described here, including the bubble size reduction or elimination, is also observed in cases where laminar separation bubbles interact with controlled periodic wake disturbances (e.g. Simoni $et\ al.\ 2012a$). In addition, the separation bubble does not exhibit any features of long bubbles (Marxen & Henningson 2011) throughout the forcing cycle, thus, the elongation represents part of a dynamic process of a short bubble.

The LSB topology is dependent on the laminar to turbulent transition process as the latter governs momentum entrainment and leads to reattachment. It is therefore expected that variations in laminar to turbulent transition within the LSB shear layer are accompanied by evident changes in integral boundary layer length scales (van Ingen 2008; Yarusevych & Kotsonis 2017). The aforementioned quantities are estimated during the forcing cycle at the streamwise location of the unforced LSB mean maximum height and are shown in figure 14. It is evident that during bursting, increasing forcing amplitude results in decrease of displacement thickness (δ^*) and increase of momentum thickness (θ). Consequently, the shape factor ($H = \delta^*/\theta$) decreases, signifying enhanced stabilisation of the boundary layer for increasing forcing amplitude, consistent with the documentations of Rist & Augustin (2006) and Marxen & Rist (2010).

Prior to the disturbance introduction ($\phi=0$), the location of maximum shape factor, H, is located in the upstream vicinity of the mean reattachment location (figures 14c and 11). This location corresponds well to the abrupt rise of wall-normal velocity fluctuations in the unforced bubble (figure 6), signifying the onset of the shear layer breakdown. Due to the low turbulence environment and the strongly inflectional profiles exhibited by the LSB, the breakdown and transition onset locations are in close proximity. As such, a first order estimation of the breakdown onset location can be derived based on the streamwise location where the shape factor is maximised. This is indicated by a square marker in figure 11. Shortly after the convection of the forced wave packet and the elimination of the LSB, the breakdown onset point swiftly shifts upstream by approximately $12\tilde{\delta}_s^*$ ($\phi=0.08$ and 0.096). Here, the absence of reverse flow leads to temporary stabilisation, which, in turn, causes the breakdown onset point to shift downstream ($\phi=0.173$). This downstream shift persists throughout the entire bursting process (figure 12). Given the observed behaviour, the phase at which the breakdown onset location is most downstream corresponds to the longest LSB ($\phi\approx0.25$), i.e. at the

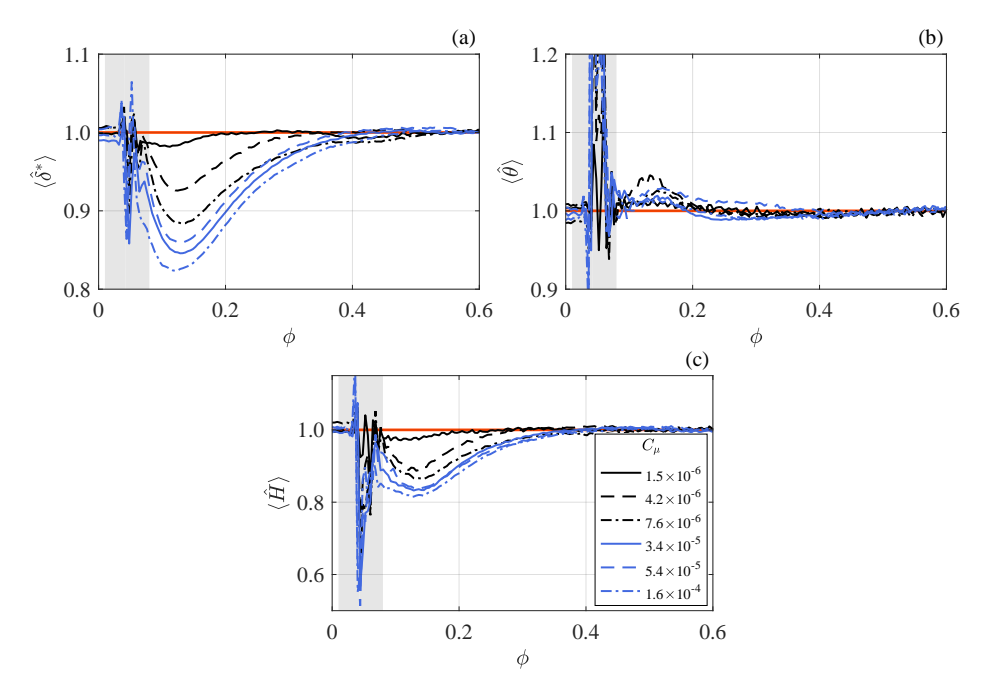


FIGURE 14. Evolution of phase-averaged boundary layer integral quantities scaled to the respective unforced value. Values are probed at the streamwise location of maximum height of the unforced LSB \bar{x}_{h_0} (a) Displacement thickness; (b) momentum thickness; (c) shape factor. Shaded region: Interval during which forced disturbance is within the field of view.

end of bursting (figure 12c). As gradual recovery ensues after maximum elongation, the breakdown onset point propagates upstream, reaching its unforced location at $\phi \approx 0.5$.

As mentioned earlier, during the interval between the bubble elimination and the end of the bursting process, the LSB shedding strength is reduced (figure 13). This notion, in conjunction with the significant changes in the breakdown onset location implies that an impulsive disturbance significantly influences the stability characteristics of the LSB. Following the elimination of the reverse flow region, the temporary stabilisation leads to reduced growth rate of incoming disturbances, thus, transition to turbulence and the associated increase of wall-normal mixing are driven to occur farther downstream. Consequently, the separated shear layer fails to reattach as early as in the unforced scenario. It is important to stress here that the apparent stabilisation of the LSB is slightly different than the one observed by Gaster (1967) and Marxen & Henningson (2011) in their respective studies. While a combination of mean flow distortion and changing amplitude of incoming instabilities was at play in the aforementioned studies, the current investigation is performed with a non-changing incoming disturbance amplitude during the bubble bursting and recovery phase.

A final comment can be given on the characteristic timescales of the observed topological changes in the LSB. As indicated by $\langle \hat{h} \rangle$ in figure 12d, increase of forcing amplitude results in faster elimination of the LSB as well as increase of the duration of reverse flow absence. Nonetheless, the phase at which the LSB recovers to its unperturbed state ($\phi \approx 0.45$) seems to be independent of the forcing amplitude. This serves as an additional indication that while the rapid and significant changes imparted on the topology and shedding behaviour of the LSB are due to the initial effect of impulsive forcing, the

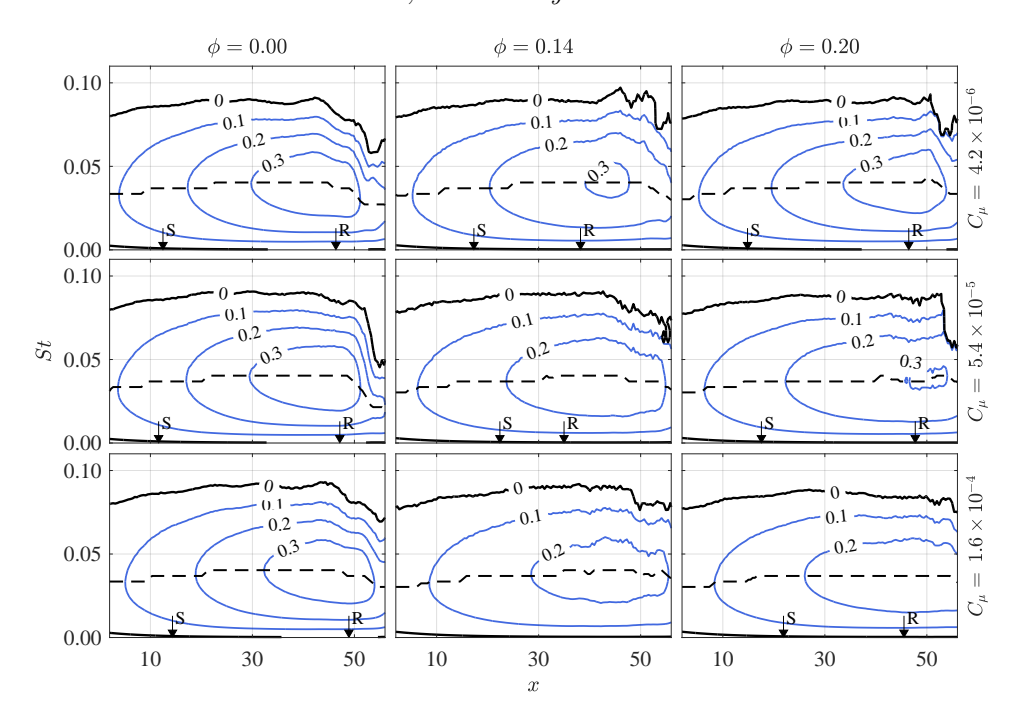


FIGURE 15. Stability diagrams for selected phases and forcing amplitudes. Solid lines: iso-contours of non-dimensional growth rate, $-\alpha_i = -\tilde{\alpha}_i \tilde{\delta}^*$. Dashed line: frequency of the most unstable mode. Separation and reattachment points are noted with S and R, respectively.

recovery to the unperturbed state is driven by the global pressure gradient and the amplitude of the natural incoming disturbances, which are constant for all tested cases.

5.2. Quasi-steady spatial stability

According to the analysis carried out in section 4.2, LST predictions (figure 9) suggest that the most amplified instability mode in the unforced LSB manifests at a frequency of approximately St=0.038 (136Hz, $\tilde{k}\tilde{h}_{\rm s}=0.78$). This is confirmed by the spectral content (figure 8) where the band of amplified frequencies ranges from St=0.022 (80Hz, $\tilde{k}\tilde{h}_{\rm s}=0.62$) to St=0.047 (170Hz, $\tilde{k}\tilde{h}_{\rm s}=0.96$). The results agree well with the findings of similar studies, e.g. Häggmark et al. (2001), $\tilde{k}\tilde{h}_{\rm s}=0.88$, Yang & Voke (2001), $\tilde{k}\tilde{h}_{\rm s}=0.98$ and Simoni et al. (2012b), $\tilde{k}\tilde{h}_{\rm s}=0.98$. In addition, as demonstrated in section 5.1, the time interval from the disturbance introduction until full recovery of the LSB is approximately $\delta\phi=0.45$, yielding an equivalent frequency of $St=1.2\times10^{-3}$ (4.4Hz). Due to this large separation of timescale between pertinent instability modes and global topology changes in the LSB, the forcing cycle may be treated as a quasi-steady process (Brevdo & Bridges 1997). In this manner, the statistical and stability properties at any given phase are considered independent of the rate of change of bubble characteristics.

The assumption of quasi-steady behaviour allows performing LST analysis as formulated in section 3.2, using phase-averaged streamwise velocity fields. Contours of growth rates for three different forcing amplitudes and selected phases within the forcing cycle are shown in figure 15. For $\phi = 0$, the growth rate fields correspond to the unforced case (figure 9a). In the following column ($\phi = 0.14$), the bubble attains its smallest size or is eliminated, depending on forcing amplitude. It is evident that the magnitude of the maximum growth rate decreases for increasing forcing amplitude, indicating increase of

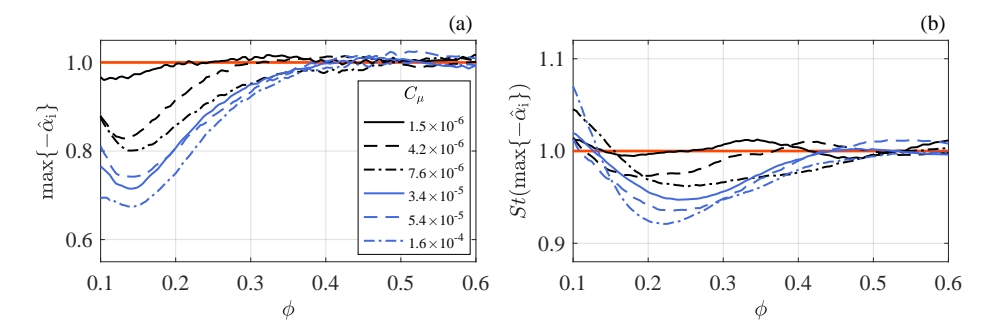


FIGURE 16. (a) Maximum growth rate and (b) most unstable frequency at \bar{x}_{h_0} for different forcing amplitudes as predicted by quasi-steady LST analysis. Quantities are normalised with the respective unforced values.

stability of the LSB, supporting observations made in section 5.1. Similar behaviour is observed for $\phi = 0.20$, during the recovery phase.

The trend for different forcing amplitudes within the forcing cycle becomes more evident by plotting the maximum growth rate at the streamwise location of the unforced LSB mean maximum height, \bar{x}_{h_0} , with respect to phase (figure 16a). Here, with reference to figure 12, it is noted that as the LSB recovers ($\phi > 0.2$) growth rates are increasing. In addition, LST calculations indicate that the frequency of the most unstable mode at the same location (figure 16b) decreases with respect to its unforced LSB value during the bubble recovery phase (0.1 < ϕ < 0.4), with a minimum achieved at $\phi \approx 0.25$. This reduction, however, is relatively small ($\approx 5\%$) compared to the respective reduction of growth rate ($\approx 25\%$), agreeing well with observations of Marxen et al. (2015).

As evident by the previous discussion, the change in mean bubble size and topology has direct consequence on stability. Reduction of the bubble height and even complete elimination of the reverse flow region results in more stable flow in LST terms. Furthermore, the effect of impulsive forcing on the integral properties of the boundary layer, such as δ^* , θ and H, appears to follow similar trend as the growth rate and frequency of most amplified mode (figure 14). The maximum growth rate as a function of the corresponding shape factor at \bar{x}_{h_0} are, therefore, shown in figure 17a for all phases during the recovery phase of the forcing cycle $(0.1 < \phi < 0.5)$ and all forcing amplitudes. For ease of comparison the values are scaled with the respective values pertaining to the unforced bubble.

It is apparent that all growth rates collapse on a monotonic, nearly-linear regression. This indicates strong correlation between stability of the LSB and integral characteristics of the boundary layer regardless of the forcing amplitude, as previously suggested in the works of LeBlanc et al. (1989), van Ingen & Kotsonis (2011) and Boutilier & Yarusevych (2012). The implication of this notion for both flapping and bursting mechanisms is a consequence of altered stability characteristics due to the influence of incoming perturbations on the bubble topology. If the perturbations are of small amplitude and intermittent, as in the case of freestream disturbances, the LSB will react with mild shape factor and stability variations leading to the observation of the flapping phenomenon. In turn, introduction of a periodic disturbance at the most unstable frequency or impulsive forcing, of amplitude higher than environmental disturbances, may achieve reduction of flapping by pegging the stability characteristics, explaining the observations of Dovgal & Boiko (1994). In the extreme case of a high amplitude impulsive disturbance, the flow distorts to an extent that the LSB diminishes and by consequence

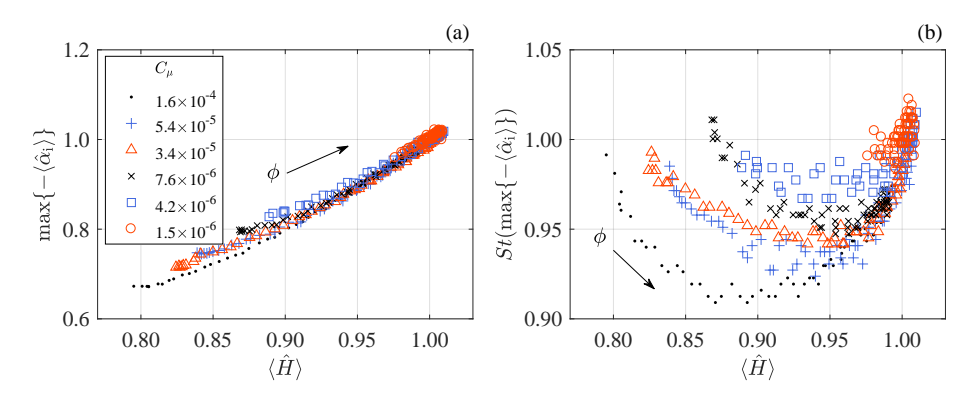


FIGURE 17. (a) Maximum growth rate and (b) most unstable frequency for different forcing amplitudes. Data are probed at \bar{x}_{h_0} and $0.1 < \phi < 0.5$ as a function of the local shape factor. All quantities are normalised with the respective unforced values.

stabilises considerably. As a result, the shear layer breakdown onset location is forced downstream (see figure 11), alleviating mixing benefits, and resulting in bubble bursting. This confirms the observations of Marxen & Henningson (2011) regarding the bursting process based on simulations where the flow becomes more stable by decreasing the amplitude of numerical unsteady forcing.

Contrary to the growth rates, the frequency of the most unstable waves is not directly proportional to the shape factor but demonstrates a parabolic variation (figure 17b). In particular, the minimum value is achieved at $\phi \approx 0.22$. With reference to the trace of the bubble length and height shown in figures 12c and 12d, this coincides with the instant when these quantities temporarily assume their unforced value, followed by the elongation due to bursting. The extremum in the frequency variation with shape factor suggests a notable change in the boundary layer characteristics. Indeed, the inflection point in the displacement thickness can be observed at the same time instant ($\phi \approx 0.22$) in figure 14a.

5.3. Disturbance characteristics

The analysis performed in the preceding sections demonstrates the strong influence of the impulsive disturbance on the LSB dynamic topology and stability. It is, therefore, imperative to describe and quantify the disturbance evolution in order to close the interaction loop. Complementary to figure 11, contours of Q-criterion (Hunt et al. 1988) are shown in figure 18 for $0.026 < \phi < 0.046$. A set of three co-rotating vortices, labelled $V_{
m p},~V_{
m u}$ and $V_{
m d},$ dominates the flow field, downstream of which the Q-criterion detects evidence of structures shed prior to the introduction of the impulse. $V_{\rm p}$ is the primary vortex produced due to the introduction of the pulse as it can be traced to the streamwise location of the actuator, x=0, at $\phi=0$. $V_{\rm d}$ is induced by $V_{\rm p}$ shortly after the impulse and becomes measurable when $V_{\rm p}$ has reached $x \approx 15$. A tertiary weaker vortex, $V_{\rm u}$, emerges upstream of V_p closing the cascade. The streamwise distance between all three vortices is initially approximately $9\delta_s^*$, however, it gradually increases to $12\delta_s^*$ between $V_{\rm p}$ and $V_{\rm d}$, as $V_{\rm d}$ passes through the accelerated flow in the reattachment region. The process closely resembles the wave packet sequence observed by Watmuff (1999). For completing characterisation of this wave packet, analysis of its frequency, convective speed and growth rate is performed.

Due to the highly transient nature of events, assessment of the frequency characteris-

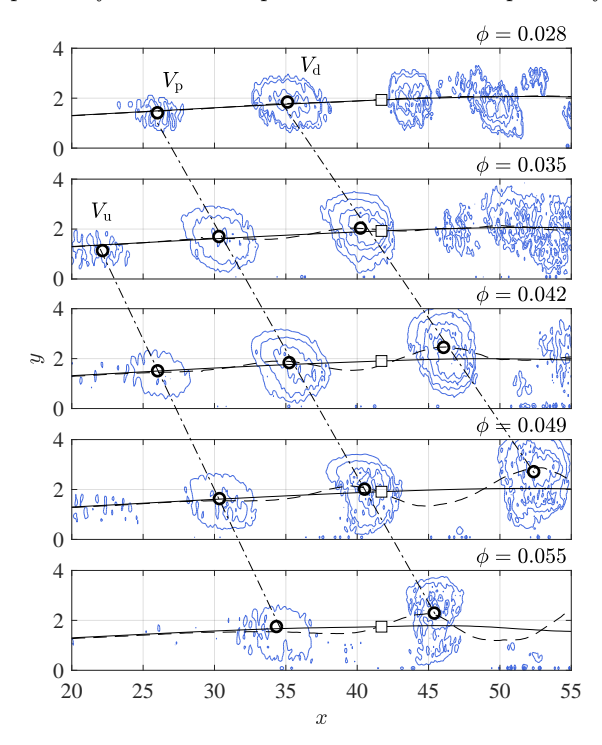


FIGURE 18. Q-criterion for $C_{\mu} = 1.6 \times 10^{-4}$ at various phases. Dashed lines: displacement thickness. Solid lines: displacement thickness based on reconstruction with $\Phi^{(1)}$ and $\Phi^{(2)}$. Dash-dot lines: connect the vortex centroids (indicated by circles) at different time instants. Square marker: location of probe used for extracting signal for wavelet analysis (figure 19).

tics of the disturbance cannot be performed via Fourier analysis. Instead, the wavelet transform is employed as described in section 3.4, on the phase-averaged vorticity signal. The disturbance is expected to affect the shape of the LSB as it convects, thus, the probe location where vorticity is extracted takes into account the deformation of the separated shear layer. Specifically, the probe's streamwise location is fixed to the location of mean maximum height of the unforced LSB, while the distance of the probe from the wall is set to the displacement thickness at the corresponding phase. In order to reduce the uncertainty in the probe location due to the passing wave packet disturbance, displacement thickness is estimated on reduced order velocity fields, reconstructed by considering POD modes $\Phi^{(1)}$ and $\Phi^{(2)}$. As demonstrated in section 3.3, these modes capture the overall motion of the bubble disregarding shedding as well as distortion of the shear layer due to the presence of the disturbance. A comparison between the displacement thickness calculated based on the full phase-averaged signal and the displacement thickness calculated on the reduced order signal (δ_{ro}^*) is shown in figure 18. The location of the probe coinciding with the reduced order displacement thickness is indicated by the square marker. The extracted vorticity signal and the corresponding wavelet coefficients for forcing amplitude of $C_{\mu} = 1.6 \times 10^{-4}$ are plotted in figure 19. Peaks in the wavelet coefficient field indicate that the dominant frequency assumed by the wave packet is approximately St = 0.037 (134Hz), which agrees with the most amplified frequency of the unforced bubble, determined from velocity spectra and LST predictions at the same streamwise position (section 4.2). It may be noted that the introduced

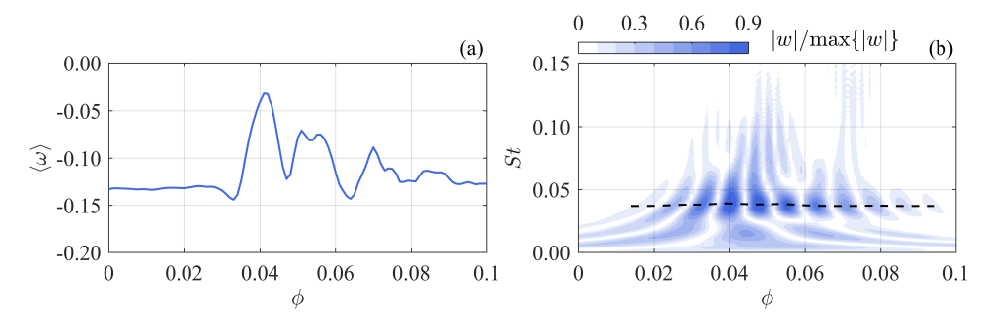


FIGURE 19. (a) Signal of phase-averaged vorticity at $x = \bar{x}_h$ and $y = \langle \delta_{ro}^* \rangle$ for $C_{\mu} = 1.6 \times 10^{-4}$. (b) Normalised wavelet coefficients. *Dashed line:* connects the maxima at each phase.

disturbance frequency maintains approximately a constant value during all the phases for which it is detected.

Though it is possible to obtain an approximation of the disturbance convective speed by tracing the propagation of the vortex cores (figure 18), a more reliable approach is followed based on integrating the phase-averaged wall-normal velocity component along the y-direction. With this method, disturbance traces are detectable even at upstream locations where the structures are still too weak to be detected by vortex identification schemes. The result is shown on an $x-\phi$ diagram in figure 20a, for the case corresponding to forcing amplitude of $C_{\mu} = 1.6 \times 10^{-4}$. Two distinct sets of convective ridges are identified. The first set is located in the interval $0 < \phi < 0.08$, spanning throughout the entire streamwise extent and pertaining to the passage of the three structures induced by the pulse $(V_p, V_d \text{ and } V_u, \text{ figure 18})$. The second set of convective ridges $(\phi > 0.2 \text{ and})$ x > 40) is the signature of the coherent vortex shedding in the aft part of the LSB, reestablished after the bursting process. Between these two regions in time $(0.08 < \phi < 0.2)$, elimination of the LSB takes place, followed by cessation of vortex shedding associated to the bursting process (see also figure 13), therefore, no clear convective ridges are observed. The convective speed of the wave packet introduced by the impulsive forcing is directly related to the slope of the dominant convective ridge (marked by the dashed line in figure 20a). The convective speed is found to be largely independent of the forcing amplitude (figure 20b) with an average value of $0.46\tilde{U}_0$, equal to estimations made on the unforced bubble (section 4.2). This is in good agreement with LST analysis predictions as well as the work of Rist & Maucher (2002) and Pröbsting & Yarusevych (2015).

Figure 20a provides an additional confirmation that the wave packet is convectively, rather than globally unstable due to the lack of ridges with negative slope that would otherwise signify upstream propagation of disturbances in the vicinity of the wall. Additionally, it is noteworthy that although data extraction is performed on phase-averaged results, evident spatial and temporal coherence due to vortex shedding is observed in the aft portion of the bubble during recovery ($\phi > 0.2$). At these phases, the artificial forcing wave packet has convected downstream and is no longer directly influencing the bubble dynamics. Consequently, the aforementioned spatio-temporal coherence indicates that bursting and the following recommencing onset of vortex shedding are associated with nearly constant time scales with respect to the impulse instant. Given that incoming disturbances during this phase intervals are effectively random, it follows that the onset of vortex shedding in a LSB that has undergone bursting is deterministically synchronised with the bursting and recovery process. This effect is not evident in the sequence presented in figure 11. This can be attributed to the limited local resolution of PIV

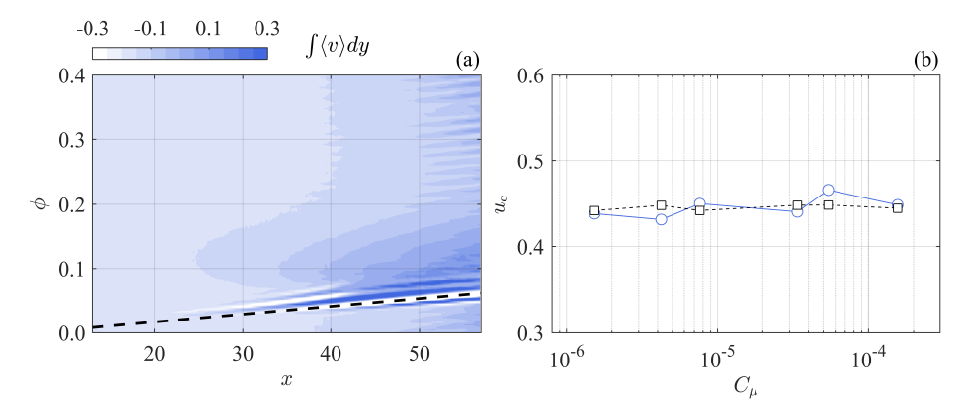


FIGURE 20. (a) Phase-streamwise location map of y-integral of wall-normal phase-averaged velocity $(\int \langle v \rangle dy)$ for $C_{\mu} = 1.6 \times 10^{-4}$. (b) Convective speed (u_c) of forced disturbance for tested forcing amplitudes. \circ : Measurements and \square : corresponding LST predictions for the most unstable mode at St = 0.043 (155Hz).

as well as insensitivity of the velocity curl to weak vortices. Nevertheless, the latter can be discerned in figure 20a due to the employed integration in the wall-normal direction.

Quantification of the growth of the introduced disturbance is based on the extraction of the phase-averaged wall-normal velocity fluctuating component, $\langle v' \rangle = \langle v \rangle - \bar{v}$, as it is not significantly affected by global shear layer fluctuation. Each of the three dominant vortical structures induced by the impulsive forcing (figure 18) features a region downstream its core where fluid is displaced towards the wall. The location where the unique local maximum magnitude of $\langle v' \rangle$ is reached within such region is recorded for phases in the interval $0.02 < \phi < 0.07$, i.e. when the wave packet is within the FOV (figure 11). Figure 21a depicts the resulting values. The magnitude of $\langle v' \rangle$ related to $V_{\rm p}$ increases as the vortex convects, reaching its peak at approximately the mean maximum height of the unforced LSB (x=42). A similar process is observed further downstream for the secondary vortex $V_{\rm d}$, although the maximum point is not captured within the current field of view. In contrast, the weaker vortex $V_{\rm u}$ induces notably lower $\langle v' \rangle$.

Comparison of the experimentally measured growth of the three individuated vortices with quasi-steady LST is enabled by extracting LST growth rates at each phase for the frequency determined through wavelet analysis (St = 0.037, 134Hz), shown as dashed lines in figure 21b. It must be noted here, that as individual vortices convect through the LSB, they experience a changing base velocity profile due to the global reduction of bubble size (figure 12). As such, each vortex is traced at a given streamwise location for each phase. A certain growth rate is predicted by LST for each pair of streamwise location and phase values. Consequently, a composite growth rate is obtained for each vortex by sliding through the phases and extracting the growth rate per streamwise location and phase where the measured $\langle v' \rangle$ is locally maximised (i.e. at each phase and corresponding streamwise location, a point is selected from the respective dashedline growth rate curve). The resulting composite growth rates correspond to the solid lines of figure 21b. A composite amplification factor, N_c , may, therefore, be estimated by integrating the composite growth rates (as per equation 3.3). Subsequently, amplification factors of the experimentally measured disturbances are derived from the logarithmic part of the same equation by setting $\tilde{A} = \langle \tilde{v}' \rangle$. Defining \tilde{A}_0 requires reformulating the left hand side of equation 3.3 as $\tilde{A}_0 = \tilde{A}/e^{N_c}$ and utilising the measured induced velocity and the aforementioned composite amplification factor at an arbitrary streamwise location

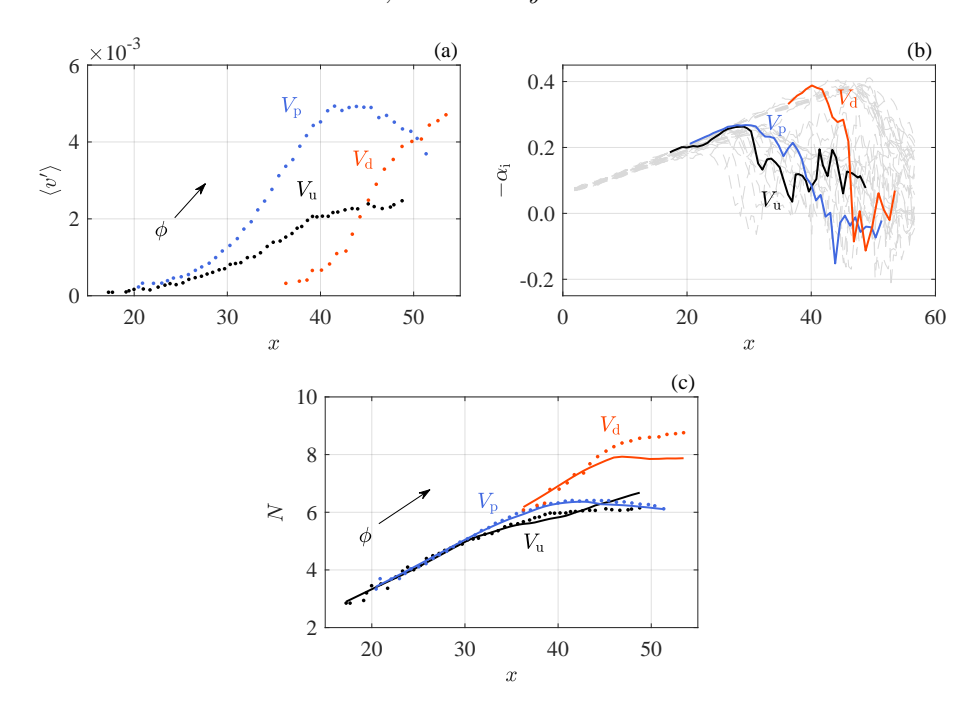


FIGURE 21. Quasi-steady LST analysis for the case of $C_{\mu} = 1.6 \times 10^{-4}$ in the phase interval $0.02 < \phi < 0.07$. (a) *Points:* magnitude of wall-directed $\langle v' \rangle$ due to forced wave packet. (b) *Dashed lines:* Non-dimensional growth rates $(-\alpha_{\rm i} = -\tilde{\alpha}_{\rm i}\tilde{\delta}^*)$ at the centre frequency determined by wavelet analysis. *Solid lines:* Composite $\alpha_{\rm i}$ based on the maximum $\langle v' \rangle$ location at each phase. (c) *Points:* N factor calculated from $\langle v' \rangle$. *Solid lines:* composite N factor calculated from the composite $\alpha_{\rm i}$.

 $(x = 30 \text{ for } V_{\text{p,u}} \text{ and } x = 40 \text{ for } V_{\text{d}})$. The constraint for this location selection is that $\langle v' \rangle$ be higher than the PIV measurement error $(\varepsilon_v \approx 2\%)$.

The two sets of growth factors are plotted in figure 21c, where point markers and solid lines correspond to measurements and quasi-steady LST respectively. Agreement between the two methods is remarkable, even when the amplitude of the experimentally measured disturbance is higher than the conventionally accepted threshold of $0.1\%U_0$ for LST (e.g. Mack 1984; Reed et al. 1996). As discussed by Diwan & Ramesh (2009), the success of LST estimations in LSBs is not fully understood. The good agreement between the two analyses shown here suggests that rather weak non-linear effects come into play for the investigated case, with little energy transferred between modes. This is traced to the impulsive nature of the forcing and the exciting of a single dominant mode, characterised by essentially constant frequency and convective speed within the bubble. The above is further enhanced by the strong two-dimensionality of the considered disturbance, pivoting on the inherent features of the plasma actuator (Kotsonis 2015). Negligible non-linear interactions appear to take place in the case of the stronger vortex $V_{\rm p}$, for which LST predictions collapse on experimental measurements for the whole streamwise extent. Contrary, for the cases of the induced $V_{\rm d}$ and $V_{\rm u}$ vortices, LST analysis diverts from measured N values at higher amplitudes, implying more substantial nonlinear interactions.

It is important to note that, as the three identified vortices convect sequentially, they experience the base flow profiles at slightly different phases (figure 18). Nevertheless, it is

evident that the amplification factor of the two advancing vortices $(V_{\rm p} \text{ and } V_{\rm d})$ increases with the same rate (i.e. slope) until approximately the mean maximum height of the unforced LSB (figure 21c). In contrast, the results for the trailing vortex $(V_{\rm u})$, which crosses the mean bubble last, indicate a notable change in growth rate slope, manifested as a 'kink' in the N factor curve, at $x \approx 30$ (figure 21c). Following figure 18, vortex $V_{\rm u}$ is at this location at phase $\phi \approx 0.05$. Indeed, again with reference to figure 18, at that instant, $V_{\rm d}$ has reached the aft part of the separation bubble. This suggests that the stability characteristics of the separated shear layer remain largely invariant during the convection of the forced wave packet. It is only when the introduced disturbance first interacts with the reattachment region that stability characteristics of the bubble are affected. The above, further reconcile with the hypothesis of a closed-loop feedback between stability, breakdown onset location and amplification of incoming disturbances suggested by Marxen & Henningson (2011).

5.4. Onset of the shear layer breakdown

Two essential features of the transitional dynamics and spatio-temporal evolution of the LSB emerge from the so-far presented analysis. These are the proportionality of the maximum growth rate to the shape factor irrespective of the incoming disturbance amplitude (section 5.2, figure 17) and the indication that stability characteristics are modified only when disturbances reach and interact with the reattachment region (section 5.3, figure 21). Both effects highlight the final stages of disturbance growth, turbulent breakdown and reattachment as the key element of the closed feedback loop, governing the flapping and bursting mechanisms.

In this section the temporal attributes of the transition process after convection of the forced disturbances are investigated. As discussed in section 5.1, for the unforced LSB the streamwise location where the shape factor is maximised may serve as a first order approximation of the onset of shear layer breakdown (figure 6). A critical amplification factor can be estimated at this streamwise position through LST, being equal to $N_{\rm crit} =$ 7.7 (figure 9). In the forced LSB cases, at each phase, incoming disturbances perceive the LSB at a certain stability state. The latter is modified as a disturbance convects downstream due to the global topological changes induced by the bursting and subsequent recovery of the bubble. This behaviour is expressed by the growth rate of the most unstable mode calculated through quasi-steady LST analysis. This is visualised in the $x-\phi$ plane by the contours of figure 22a. Evidently, any given disturbance convecting through the domain will experience a local growth rate corresponding to both the current streamwise location of the disturbance (x) and phase (ϕ) . Based on this observation and given the established nearly-constant convective speed of $0.46U_0$ (figure 20), a composite growth rate, $-\alpha_{i_{comp}}$, can be constructed for a given disturbance entering the domain at phase ϕ . The trajectories of such disturbances through the $x-\phi$ plane (loci of $-\alpha_{\text{icomp}}$) are visualised by exemplary dashed lines in figure 22a, the slope of which is equal to the convective speed. Composite growth rate curves are extracted only for disturbances entering after the propagation of the wave packet ($\phi > 0.08$).

A comparison is now performed between LST predictions for breakdown onset and the experimental measurements. Direct estimations of the streamwise location where the shape factor is maximised (i.e. onset of breakdown) may be done from the phase-averaged velocity data (figure 11) and are marked by a dashed line in figure 22b. Additionally, integration of the composite growth rates (figure 22a) provides composite N factor curves, $N_{\text{comp}}(x,\phi)$, (as per equation 3.3). Subsequently, the value of N_{comp} is extracted for each phase at the x-location of maximum H. The result is traced by the solid line in figure 22 and is complementary to the observations analysed in section 5.1 and figure 11. It is

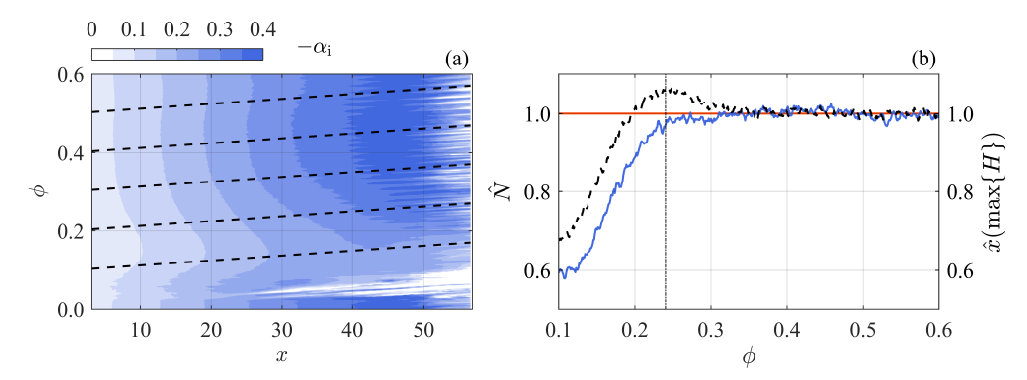


FIGURE 22. Quasi-steady LST analysis for the case of $C_{\mu} = 1.6 \times 10^{-4}$. (a) Growth rates $(-\alpha_{\rm i} = -\tilde{\alpha}_{\rm i}\tilde{\delta}^*)$ of mode with St = 0.043 (155Hz), with respect to phase and streamwise location. Dashed lines: Loci of composite growth rates $(-\alpha_{\rm icomp})$ for disturbances convecting at speed of $0.46\tilde{U}_0$. (b) Dashed line: Evolution of the measured streamwise location of maximum shape factor, $x(\max\{H\})$; Solid line: LST-predicted N-factor at the streamwise location of maximum shape factor calculated from $\alpha_{\rm icomp}$; Dash-dot line: End of the bursting process $(\phi \approx 0.24)$.

evident that the convection of the initial forced wave packet over the aft portion of the bubble ($\phi \approx 0.1$) is followed by a significant decrease in the amplification factor with respect to its unforced LSB value ($\sim 0.55N_{\rm crit}$). The flow is, therefore, becoming more stable, in line with the results of the analysis carried out in section 5.2.

6. Summary and concluding remarks

An experimental investigation of the spatial and temporal response of a laminar separation bubble to impulsive forcing is carried out by means of time-resolved PIV and linear stability theory. The LSB develops on a flat plate, driven by an imposed adverse pressure gradient at a Reynolds number based on the separation point displacement thickness of $Re_{\delta_s^*}=1305$. The aim is providing insight into both flapping and bursting mechanisms of a short LSB by deterministically forcing the dynamics of the bubble. The selection of impulsive forcing allows excitation of natural modes through selective amplification (Gaster 1967) as well as further development of the flow in natural disturbance conditions. Introduction of disturbances is spanwise and two-dimensional, achieved by means of an AC-DBD plasma actuator, located just upstream of the mean separation point of the unforced LSB. The forcing amplitude spans over two orders of magnitude when expressed in terms of momentum coefficient and is varied by adjusting the DBD voltage. The forcing of the bubble with well-separated impulsive pulses facilitates phase-averaged analysis.

Following its introduction, the impulsive disturbance undergoes convective amplification as it propagates along the separated shear layer, evolving into a wave packet, similar to the results of Watmuff (1999). Once the latter has convected past the reattachment point, the LSB rapidly shrinks from both upstream and downstream sides. If the forcing amplitude is sufficiently high, the separation bubble is completely eliminated. This rapid process is followed by a gradual recovery in the bubble length similar to the bubble bursting process. Recovery to the unperturbed state is shown to be achieved at the same phase regardless of the forcing amplitude, further reconciling with the principle of impulsive forcing.

The timescale difference between pertinent instability modes derived from LST analysis and measured global topology changes of the LSB during the forcing cycle allow for

treating the latter as a quasi-steady process (Brevdo & Bridges 1997). Pivoting on this observation, LST calculations are performed on phase-averaged velocity fields. After the elimination of the LSB, the amplification rate and the frequency of the predicted most unstable mode are found to decrease with increasing forcing amplitude. The same trend is followed by boundary layer integral quantities and, therefore, when the maximum growth rate is compared to the shape factor, the two quantities collapse on a monotonic linear regression for all forcing amplitudes. The aforementioned correlation confirms the conjecture that both flapping and bursting mechanisms are driven by altered stability characteristics due to the influence of incoming disturbances of different amplitude. Contrary to the growth rate, the frequency of the most unstable wave is not monotonic with respect to the shape factor but rather exhibits a parabolic relation.

Analysis of the wave packet produced by the impulse is performed for estimating frequency, convective speed and growth rate. The transient nature of the disturbance dictates the use of wavelet analysis for estimating the frequency of the wave packet. As expected, the frequency assumed is equal to the LSB shedding frequency, both from the comparison with velocity spectra and LST analysis of the unforced bubble. The convective speed is determined to be constant regardless of the forcing amplitude $(0.46\tilde{U}_0)$. Regarding the wave packet amplification, a remarkable agreement between measurements and LST is observed. The estimated growth of the vortices comprising the wave packet is shown to change once they start interacting with the breakdown region. This implies that stability changes ensue only when disturbances gain significant amplitudes and affect the flow in the aft portion of the LSB.

Variation of stability due to interactions of disturbances with the shear layer breakdown process stresses the necessity of investigating temporal attributes of the latter. The convection of the wave packet is followed by a significant reduction of the amplification factor, indicating flow stabilisation. At the same time, the breakdown onset location where the shape factor is maximised shifts upstream.

In conclusion, experimental evidence has been provided for coupling incoming disturbances with the LSB shear layer breakdown location and, consequently, with changes in stability characteristics towards flow stabilisation. This feedback loop serves as a ground for both flapping and bursting mechanisms and is paramount for active flow control realisation.

REFERENCES

- Alam, M. & Sandham, N. D. 2000 Direct numerical simulation of "short" laminar separation bubble with turbulent reattachment. *Journal of Fluid Mechanics* 410, 1–28.
- AMITAY, M., SMITH, D. R., KIBENS, V., PAREKH, D.E. & GLEZER, A. 2001 Aerodynamic flow control over an unconventional airfoil using synthetic jet actuators. *AIAA Journal* **39** (3), 361–370.
- Bake, S., Meyer, D. G. W. & Rist, U. 2002 Turbulence mechanism in Klebanoff transition: a quantitative comparison of experiment and direct numerical simulation. *Journal of Fluid Mechanics* **459**, 217–243.
- Benard, N. & Moreau, E. 2014 Electrical and mechanical characteristics of surface ac dielectric barrier discharge plasma actuators applied to airflow control. *Experiments in Fluids* **55** (11).
- BOIKO, A. V., GREK, G. R., DOVGAL, A. V & KOZLOV, V. V. 2002 The origin of Turbulence in Near-Wall Flows. Springer.
- BOUTILIER, M. S. H. & YARUSEVYCH, S. 2012 Separated shear layer transition over an airfoil at a low Reynolds number . *Physics of Fluids* **24** (084105).
- Brevdo, L. & Bridges, T. J. 1997 Local and global instabilities of spatially developing

- flows: cautionary examples. Proceedings of the Royal Society of London A: Mathematical, Physical and Engineering Sciences 453 (1962), 1345–1364.
- CORKE, T. C., ENLOE, C. L. & WILKINSON, S. P. 2010 Dielectric barrier discharge plasma actuators for flow control. *Annual Review of Fluid Mechanics* **42**, 505–529.
- Daubechies, I. 1992 Ten Lectures on Wavelets, CBMS-NSF Regional Conference Series in Applied Mathematics, vol. 61. SIAM.
- DIWAN, S. S. & RAMESH, O. N. 2009 On the origin of the inflectional instability of a laminar separation bubble. *Journal of Fluid Mechanics* **629**, 263–298.
- DOVGAL, A. V & BOIKO, A. V. 1994 Effect of harmonic excitation on instability of a laminar separation bubble on an airfoil. In *Laminar-Turbulent Transition* (ed. H. F. Fasel & W. S. Saric), pp. 675–680. Springer.
- DOVGAL, A. V., KOZLOV, V. V. & MICHALKE, A. 1994 Laminar boundary layer separation: Instability and associated phenomena. *Progress in Aerospace Sciences* **30** (1), 61–94.
- FARGE, M. 1992 Wavelet transforms and their applications to turbulence. *Annual Review of Fluid Mechanics* **24**, 395–457.
- GASTER, M. 1967 The Structure and Behaviour of Laminar Separation Bubbles. *Tech. Rep.* 3595. Aeronautical Research Council Reports and Memoranda.
- Gaster, M. 1992 Instability, Transition, and Turbulence, chap. Stability of Velocity Profiles with Reverse Flow, pp. 212–215. New York, NY: Springer New York.
- GASTER, M. & GRANT, I. 1975 An experimental investigation of the formation and development of a wave packet in a laminar boundary layer. *Proceedings of the Royal Society of London A: Mathematical, Physical and Engineering Sciences* **347**, 253–269.
- HÄGGMARK, C. P., HILDINGS, C. & HENNINGSON, D. S. 2001 A numerical and experimental study of a transitional separation bubble. *Aerospace Science and Technology* 5 (5), 317–328.
- HAIN, R., KÄHLER, C. J. & RADESPIEL, R. 2009 Dynamics of laminar separation bubbles at low-reynolds-number aerofoils. *Journal of Fluid Mechanics* **630**, 129–153.
- Ho, C. M. & Huerre, P. 1984 Perturbed free shear layers. Annual Review of Fluid Mechanics 16, 365–424.
- HUNT, J. C. R., WRAY, A. & MOIN, P. 1988 Eddies, Stream, and Convergence Zones in Turbulent Flows. *Tech. Rep.* CTR-S88. Center For Turbulence Research.
- VAN INGEN, J. L. 2008 The e^N method for transition prediction. Historical review of work at TU Delft. In 38th Fluid Dynamics Conference and Exhibit. Seattle, WA.
- VAN INGEN, J. L. & KOTSONIS, M. 2011 A two-parameter method for e^N transition prediction. In 6th AIAA Theoretical Fluid Mechanics Conference. Honolulu, HI.
- Jones, L. E., Sandberg, R. D. & Sandham, N. D. 2010 Stability and receptivity characteristics of a laminar separation bubble on an aerofoil. *Journal of Fluid Mechanics* **648**, 257–296.
- Jones, L. E., Sandbergh, R. D. & Sandham, N. D. 2008 Direct numerical simulation of forced and unforced separation bubbles on an airfoil at incidence. *Journal of Fluid Mechanics* **602**, 175–207.
- KÄHLER, C. J., SCHARNOWSKI, S. & CIERPKA, C. 2012 On the resolution limit of digital particle image velocimetry. *Experiments in Fluids* **52**, 1629–1639.
- VON KERCZEK, C. & DAVIS, S. H. 1974 Linear stability theory of oscillatory stokes layers. Journal of Fluid Mechanics 62, 753–773.
- Kotsonis, M. 2015 Diagnostics for characterisation of plasma actuators. Measurement Science and Technology ${f 26}$ (9).
- Kotsonis, M., Ghaemi, S., Veldhuis, L. L. M. & Scarano, F. 2011 Measurement of the body force field of plasma actuators. *Journal of Physics D: Applied Physics* 44 (4).
- KURELEK, J. W., LAMBERT, A. R. & YARUSEVYCH, S. 2016 Coherent Structures in the Transition Process of a Laminar Separation Bubble. *AIAA Journal* **54** (8), 2295–2309.
- Leblanc, P., Blackwelder, R. & Liebeck, R. 1989 A Comparison Between Boundary Layer Measurements in a Laminar Separation Bubble Flow and Linear Stability Theory Calculations, pp. 189–205. Berlin, Heidelberg: Springer Berlin Heidelberg.
- Lengani, D., Simoni, D., Ubaldi, M. & Zunino, P. 2014 POD analysis of the unsteady behavior of a laminar separation bubble. *Experimental Thermal and Fluid Science* 58, 70–79.

- LIN, N., REED, H. L. & SARIC, W. S. 1992 Effect of leading-edge geometry on boundary-layer receptivity to freestream sound, Instability, Transition and Turbulence. New York: Springer-Verlag.
- Mack, L. M. 1984 Boundary-layer linear stability theory. Tech. Rep. 709. AGARD.
- MARXEN, O. & HENNINGSON, D. S. 2011 The effect of small-amplitude convective disturbances on the size and bursting of a laminar separation bubble. *Journal of Fluid Mechanics* **671**, 1–33.
- MARXEN, O., KOTAPATI, R. B., MITAL, R. & ZAKI, T. 2015 Stability analysis of separated flows subject to control by zero-net-mass-flux jet. *Physics of Fluids* **27** (2), 024107.
- MARXEN, O., LANG, M. & RIST, U. 2013 Vortex formation and vortex breakup in a laminar separation bubble. *Journal of Fluid Mechanics* **728**, 58–90.
- MARXEN, O., LANG, M., RIST, U., LEVIN, O. & HENNINGSON, D. S. 2009 Mechanisms for spatial steady three-dimensional disturbance growth in a non-parallel and separating boundary layer. *Journal of Fluid Mechanics* **634**, 165–189.
- MARXEN, O. & RIST, U. 2010 Mean flow deformation in a laminar separation bubble: Separation and stability characteristics. *Journal of Fluid Mechanics* **660**, 37–54.
- Monkewitz, P. A. & Huerre, P. 1982 The influence of the velocity ratio on the spatial instability of mixing layers. *Physics of Fluids* **25**, 1137–1143.
- NIEW, T. R. 1993 The stability of the flow in a laminar separation bubble. PhD thesis, Cambridge University.
- OWEN, P. R. & KLANFER, L. 1955 On the laminar boundary layer separation from the leading edge of a thin airfoil. *Tech. Rep.* C.P. 220. Aeronautical Reseach Council, UK.
- Pauley, L. L., Moin, P. & Reynolds, W. C. 1990 The structure of two-dimensional separation. *Journal of Fluid Mechanics* **220**, 397–411.
- Pereira, R., Ragni, D. & Kotsonis, M. 2014 Effect of external flow velocity on momentum transfer of dielectric barrier discharge plasma actuators. *Journal of Applied Physics* 116 (10).
- PRÖBSTING, S. & YARUSEVYCH, S. 2015 Laminar separation bubble development on an airfoil emitting tonal noise. *Journal of Fluid Mechanics* **780**, 167–191.
- Reed, H. L., Saric, W. S. & Arnal, D. 1996 Linear stability theory applied to boundary layers. *Annual Review of Fluid Mechanics* 28, 389–428.
- REYNOLDS, W. C. & HUSSAIN, A. K. M. F. 1972 The mechanics of an organised wave in turbulent shear flow. part 3. theoretical models and comparisons with experiments. *Journal of Fluid Mechanics* **54**, 263–288.
- RIST, U. & AUGUSTIN, K. 2006 Control of laminar separation bubbles using instability waves. AIAA Journal 44 (10), 2217–2223.
- RIST, U. & MAUCHER, U. 2002 Investigations of time-growing instabilities in laminar separation bubbles. European Journal of Mechanics, B/Fluids 21 (5), 495–509.
- Sandham, N. D. 2008 Transitional separation bubbles and unsteady aspects of aerofoil stall. The Aeronautical Journal 112, 395–404.
- SARIC, W. S. & WHITE, E. 1998 Influence of high-amplitude noise on boundary-layer transition to turbulence. $AIAA\ Journal\ 98-2645.$
- Scarano, F. & Riethmuller, M.L. 2000 Advances in iterative multigrid PIV image processing. *Experiments in Fluids* **29** (SUPPL. 1), S51–S60.
- SERNA, J. & LÁZARO, B. J. 2014 The final stages of transition and the reattachment region in transitional separation bubbles. *Experiments in Fluids* **55** (4).
- Serna, J. & Lázaro, B. J. 2015 On the bursting condition for transitional separation bubbles. Aerospace Science and Technology 44, 43–50.
- Simoni, D., Ubaldi, M., Zunino, P. & Bertini, F. 2012a Transition mechanisms in laminar separation bubbles with and without incoming wakes and synthetic jets. *Experiments in Fluids* **53**, 173–186.
- Simoni, D., Ubaldi, M., Zunino, P., Lengani, D. & Bertini, F. 2012b An experimental investigation of the separated-flow transition under high-lift turbine blade pressure gradients. Flow Turbulence and Combustion 88, 45–62.
- SIROVICH, L. 1987 Turbulence and the dynamics of coherent structures. I Coherent structures. II - Symmetries and transformations. III - Dynamics and scaling. Quarterly of Applied Mathematics 45, 561–571, 573–590.

- Tani, I. 1964 Low-speed flows involving bubble separations. *Progress in Aerospace Sciences* 5, 70–103.
- Theofilis, V. 2011 Global linear instability. Annual Review of Fluid Mechanics 43, 319–352.
- Theofilis, V., Hein, S. & Dallmann, U. 2000 On the origins of unsteadiness and three-dimensionality in a laminar separation bubble. *Philosophical Transactions of the Royal Society of London A: Mathematical, Physical and Engineering Sciences* **358** (1777), 3229–3246
- Watmuff, J. H. 1999 Evolution of a wave packet into vortex loops in a laminar separation bubble. *Journal of Fluid Mechanics* **397**, 119–169.
- Welch, P. 1967 The use of fast Fourier transform for the estimation of power spectra: A method based on time averaging over short, modified periodograms. *IEEE Transactions on Audio and Electroacoustics* 15, 70–73.
- WIENEKE, B. 2015 PIV uncertainty quantification from correlation statistics. *Measurement Science and Technology* **26** (7), 074002.
- Yang, Z. & Voke, P. R. 2001 Large-eddy simulation of boundary-layer separation and transition at a change of surface curvature. *Journal of Fluid Mechanics* **439**, 305–333.
- Yarusevych, S. & Kotsonis, M. 2017 Effect of Local DBD Plasma Actuation on Transition in a Laminar Separation Bubble. Flow, Turbulence and Combustion pp. 1–22.
- Yarusevych, S., Sullivan, P. E. & Kawall, J. G. 2007 Effect of acoustic excitation amplitude on airfoil boundary layer and wake development. *AIAA Journal* **45** (4), 760–771
- Yarusevych, S., Sullivan, P. E. & Kawall, J. G. 2009 On vortex shedding from and airfoil in low-reynolds-number flows. *Journal of Fluid Mechanics* **632**, 245–271.
- ZAMAN, K. B. M. Q., MCKINZIE, D. J. & RUMSEY, C. L. 1989 Natural low-frequency oscillation of the flow over an airfoil near stalling conditions. *Journal of Fluid Mechanics* **202**, 403–442.